Machine Learning Approaches to Improving the Transient Stability of Voltage-Source Converters in Weak Grids

Amir Sepehr

Machine Learning Approaches to Improving the Transient Stability of Voltage-Source Converters in Weak Grids

Amir Sepehr

A doctoral thesis completed for the degree of Doctor of Science (Technology) to be defended, with the permission of the Aalto University School of Electrical Engineering, at a public examination held at the lecture hall AS1 of Maarintie 8 on 28 April 2023 at 12:00.

Aalto University
School of Electrical Engineering
Department of Electrical Engineering and Automation
Renewable Energies for Power Systems

Supervising professor
Prof. Edris Pouresmaeil, Aalto University, Finland

Thesis advisor
Prof. Mikko Routimo, Aalto University, Finland

Preliminary examiners
Prof. Hasan Mehrjerdi, Qatar University, Qatar
Prof. Eduardo Prieto-Araujo, Polytechnic University of Catalonia (UPC), Spain

Opponent
Prof. Sergio Vazquez Perez, University of Seville, Spain

NORDIC SWAN ECOLABEL
Printed matter
4041-0619

Author
Amir Sepehr

Name of the doctoral thesis
Machine Learning Approaches to Improving the Transient Stability of Voltage-Source Converters in Weak Grids

Abstract

With the proliferation of converter-interfaced generation in modern power systems, grid-forming converters are viewed as a solution to improve system stability and resilience in weak power grids. However, the dynamic behaviour of the grid-converter systems is strongly influenced by inevitable disturbances and transients in weak power grids (e.g. short circuit faults). Moreover, grid-converter systems are prone to harmonic instability due to the interactions between the converters and passive elements. These issues pose security risks and limit the further integration of renewable generation into the modern power system. Therefore, this thesis aims to improve the transient stability and harmonic stability of grid-converter systems by employing deep-learning and analytic methods for developing power synchronization control (PSC) in weak power grids. First, the internal structure of the synchronization loop in PSC is modified to reduce vulnerability to grid transients by utilizing a back-calculation scheme. Also, the damping characteristics of PSC are enhanced to mitigate the decaying DC offset current of the converter. Second, the internal reference calculation is developed by embedding a long short-term memory (LSTM) neural network into PSC. The LSTM neural network is trained to extract and predict the grid voltage trajectory based on the converter dynamics and grid strength. Thus, the control system updates the internal references dynamically to meet the low-voltage ride-through (LVRT) requirements and prevent synchronization loss. Third, by employing deep learning methods and neural networks, an encoder-stacked classifier is introduced for early detection of synchronization instability. This allows time for corrective control actions to be taken and prevents synchronization loss in the grid-converter system. The applied neural networks are trained to be robust against data corruption and added noise. Finally, the admittance characteristics of converters are studied and necessary conditions are outlined for achieving harmonic stability with PSC in weak grids. Moreover, a 12.5-kVA three-phase back-to-back converter system is implemented under weak grid conditions for the experimental evaluation of the results and future works.

Preface

I would like to begin by expressing my gratitude to Prof. Edris Pouresmaeil for providing me with the opportunity to contribute to an ongoing research project focused on the application of deep learning methods in the control of power-electronic converters. I am deeply grateful to Prof. Pouresmaeil for his consistent support and guidance throughout my doctoral studies.

I would like to extend my sincere thanks to Prof. Oriol Gomis-Bellmunt for his invaluable collaboration on this research project and for accepting me as a visiting doctoral researcher at the Centre of Technological Innovation in Power Electronics and Drives (CITCEA), Polytechnic University of Catalonia (UPC), Spain. Also, I take great pleasure in thanking Dr. Mikko Routimo for his indispensable guidance and support as the thesis advisor. Additionally, I would like to thank my former and current colleagues and the department staff for creating a wonderful working environment.

Lastly, I would like to express my heartfelt appreciation to my parents and my love, Bahareh, for their unwavering support and encouragement throughout my academic journey. Their love and motivation have been an endless source of inspiration, and I am truly blessed to have them in my life.

Espoo, February 26, 2023,

Amir Sepehr

Contents

List of Publications

This thesis consists of an overview and of the following publications which are referred to in the text by their Roman numerals.

I Amir Sepehr, Oriol Gomis-Bellmunt, Edris Pouresmaeil. Employing Machine Learning for Enhancing Transient Stability of Power Synchronization Control During Fault Conditions in Weak Grids. *IEEE Transactions on Smart Grid*, vol. 13, issue 3, pp. 2121-2131, May 2022.

II Amir Sepehr, Mobina Pouresmaeil, Edris Pouresmaeil. Enhancing Transient Stability of Power Synchronization Control via Deep Learning. In *23rd European Conference on Power Electronics and Applications (EPE'21 ECCE Europe)*, Ghent, Belgium, pp. 1-10, September 2021.

III Amir Sepehr, Mobina Pouresmaeil, Mojgan Hojabri, Frede Blaabjerg, Edris Pouresmaeil. Improving Transient Stability of Power Synchronization Control for Weak Grid Applications. In *IEEE 21st Workshop on Control and Modeling for Power Electronics (COMPEL)*, Aalborg, Denmark, pp. 1-6, November 2020.

IV Amir Sepehr, Mobina Pouresmaeil, Edris Pouresmaeil. Harmonic Stability Analysis of Grid-Connected Converters with Power Synchronization Control. In *IEEE PES Innovative Smart Grid Technologies Europe (ISGT Europe)*, Espoo, Finland, pp. 1-6, October 2021.

V Mobina Pouresmaeil, Amir Sepehr, Reza Sangrody, Shamsodin Taheri, Edris Pouresmaeil. Control of Multilevel Converters for High Penetration of Renewable Energies. In *IEEE 12th International Symposium on Power Electronics for Distributed Generation Systems (PEDG)*, Chicago, IL, USA, pp. 1-5, June-July 2021.

VI Mobina Pouresmaeil, Meysam Saeedian, Amir Sepehr, Reza Sangrody, Edris Pouresmaeil. Fault-Ride-Through Capability of VSG-Based Grid-Forming Converters. In *23rd European Conference on*

Power Electronics and Applications (EPE'21 ECCE Europe), Ghent, Belgium, pp. 1-7, September 2021.

VII Mobina Pouresmaeil, Amir Sepehr, Basit Ali khan, Jafar Adabi, Edris Pouresmaeil. Model predictive-based control technique for fault-ride-through capability of VSG-based grid-forming converter. In *24th European Conference on Power Electronics and Applications (EPE'22 ECCE Europe)*, Hannover, Germany, pp. 1-6, September 2022.

Author's contributions

Publication I: "Employing Machine Learning for Enhancing Transient Stability of Power Synchronization Control During Fault Conditions in Weak Grids"

The author designed the research concept, formulated the problem, developed the learning and control algorithms, designed the experiments, and wrote the paper. Prof. Edris Pouresmaeil supervised the research and Prof. Oriol Gomis-Bellmunt contributed by commenting on the manuscript.

Publication II: "Enhancing Transient Stability of Power Synchronization Control via Deep Learning"

The author designed the research concept, performed simulations and analyses, and wrote the paper under the guidance of Prof. Edris Pouresmaeil. Ms. Mobina Pouresmaeil contributed by helping with the simulations and participating in the writing of the manuscript.

Publication III: "Improving Transient Stability of Power Synchronization Control for Weak Grid Applications"

The author developed the control scheme, performed simulations and analyses, and wrote the paper under the guidance of Prof. Edris Pouresmaeil. Ms. Mobina Pouresmaeil participated in the writing and reviewing of the manuscript. Dr. Mojgan Hojabri and Prof. Frede Blaabjerg contributed by commenting on the manuscript.

Publication IV: "Harmonic Stability Analysis of Grid-Connected Converters with Power Synchronization Control"

The author developed the model, conducted simulations, analyzed the results, and prepared the paper under the guidance of Prof. Edris Pouresmaeil. Ms. Mobina Pouresmaeil contributed by participating in the writing and reviewing of the manuscript.

Publication V: "Control of Multilevel Converters for High Penetration of Renewable Energies"

The author contributed by helping with the simulation, preparing the test bench for grid-forming features, and participating in the writing and reviewing of the manuscript. Ms. Mobina Pouresmaeil designed the research concept, carried out the simulations, and prepared the research paper under the guidance of Prof. Edris Pouresmaeil. Prof. Shamsodin Taheri and Dr. Reza Sangrody contributed by commenting on the manuscript.

Publication VI: "Fault-Ride-Through Capability of VSG-Based Grid-Forming Converters"

The author contributed by helping with the simulation and comparison of conventional fault-current limitation methods in grid-forming converters and reviewing the manuscript. Ms. Mobina Pouresmaeil designed the research concept, performed simulations and analyses, and wrote the paper under the guidance of Prof. Edris Pouresmaeil. Mr. Meysam Saeedian and Dr. Reza Sangrody contributed by commenting on the manuscript.

Publication VII: "Model predictive-based control technique for fault-ride-through capability of VSG-based grid-forming converter"

The author contributed by helping with the simulation, preparing the test bench for the fault-ride-through capability of a grid-forming converter, and reviewing the manuscript. Ms. Mobina Pouresmaeil carried out the analysis and simulations and prepared the research paper under the guidance of Prof. Edris Pouresmaeil. Prof. Jafar Adabi and Mr. Basit Ali khan contributed by commenting on the manuscript.

Abbreviations

AC	Alternating current
ADC	Analog-to-digital converter
CC	Current controller
CIR	Converter-interfaced renewable
CNN	Convolutional neural networks
DC	Direct current
ETS	Enhanced transient stability
ESC	Encoder-stacked classifier
FC	Fully connected
GFL	Grid-following
GFM	Grid-forming
L	Inductor (filter)
LC	Inductor-capacitor (filter)
LCL	Inductor-capacitor-inductor (filter)
LOS	Loss of synchronization
LSTM	Long short-term memory
LVRT	Low-voltage ride-through
MLP	Multi-layer perceptron
MSE	Mean squared error
NRMSE	Normalized root mean square error

PCA	Principal component analysis
PCC	Point of common coupling
PI	Proportional integral
PIC	Power-injection collapse
PLL	Phase-locked loop
PR	Proportional resonant
PSC	Power synchronization control
PSCS	Power synchronization control scheme
PSL	Power synchronization loop
PWM	Pulse width modulation
RAP	Reverse active power
RES	Renewable energy source
ReLU	Rectified linear unit
RMS	Root mean square
RMSE	Root mean squared error
SCR	Short circuit ratio
SG	Synchronous generator
SPC	Synchronous power controller
SRF	Synchronous reference frame
tSNE	t-Distributed stochastic neighbor embedding
VC	Vector control
VSC	Voltage source converter
VSM	Virtual synchronous machine

Symbols

Uppercase and lowercase boldface symbols indicate matrices and vectors, respectively. Vectors with complex values in the synchronous reference frame are denoted by boldface symbols with the superscript dq. Noise-containing data samples are marked with a tilde. Variables that have been reconstructed or estimated are marked with a hat. Limited variables are marked with an overline. Values marked with the subscript ref are reference values.

$b_m,\ \hat{b}_n$	Bias terms in trained neural networks
$\mathbf{b}_{M\times 1},\ \hat{\mathbf{b}}_{L\times 1}$	Matrices of bias terms
$C_{\mathrm{ac}}(s),\ C_{\mathrm{Q}}(s)$	Controllers of alternating voltage and reactive power
$D(s)$	High-pass filter for active damping
$e_{\mathrm{a}}(t),\ e_{\mathrm{b}}(t),\ e_{\mathrm{c}}(t)$	Internal balanced phase voltage of converter
$f,\ f_{\mathrm{enc}},\ f_{\mathrm{dec}}$	Squashing function in trained neural networks
$G_d,\ G_{\mathrm{D}},\ G_{\mathrm{PWM}}$	Transfer functions of damping, delay and PWM
$\mathbf{h}$	Hidden layer vector of autoencoder network
$H(s)$	High-pass filter for damping
$H_{\mathrm{ETS}}(s)$	Second-order high-pass filter for damping in ETS-PSC
$\mathbf{i}^{\mathrm{dq}}$	Converter current vector in SRF
$J\left(\mathbf{W}, \mathbf{b}, \hat{\mathbf{W}}, \hat{\mathbf{b}}\right)$	Data reconstruction cost function
$J_{\mathrm{P}\theta}(s)$	Linearized dynamic model of delivered active power
K_{ip}	Integrator gain of PSL
K_{iv}	Integrator gain of AC voltage controller
k_{d}	High-pass filter gain

Symbols

L	Number of samples in each time-series of sampled data
L_{eq}	Equivalent fault inductance
L_{filter}, L_{LCL}	Equivalent inductance of LCL filter
L_{line1}, L_{line2}	Inductance values of transmission lines
$L_{\text{Minor}}(s)$	Minor-loop transfer function
L_{T}	Equivalent inductance of transmission system
L_{trans}	Inductance of transformer
M	Number of neurons in encoder
N_{Ins}	Number of unstable cases studied
N_{Sta}	Number of stable cases studied
N_{Total}	Total number of cases studied
N_{Tr}	Number of cases used for training
N_{Val}	Number of cases used for validation
P_{g}, P_{pcc}	Measured output active power at PCC
$P_{\text{g,Q}}$	Calculated active power during reactive power injection
P_{ref}	Active power reference
Q, Q_{ref}	Measured reactive power and reactive power reference
r_{eq}	Equivalent system resistance
R_{eq}	Equivalent fault resistance
R_{d}	Active resistance for damping
t_{crt}	critical fault-clearance time
T_{s}, T_{w}	Sampling period and sampling window
U_{bus}	Infinite bus voltage
U_{pcc}, U_{ref}	Measured PCC voltage and PCC voltage reference
V_0	Grid nominal voltage
V_{C}, V_{G}	RMS line-to-line voltages of grid and converter
$\mathbf{v}$, $\tilde{\mathbf{v}}$	Vectors of sampled voltages and corrupted samples
$\hat{\mathbf{v}}$, $\hat{v}_n$	Vector and elements of reconstructed data

$\hat{V}$	Internal voltage amplitude of converter
$V_{\mathrm{pcc,ref}}$	PCC voltage reference
$\mathbf{V}_{\mathrm{ref}}^{\mathrm{dq}}$	Converter-voltage reference vector in SRF
$|v_{\mathrm{pcc}}|$	Measured voltage amplitude at PCC
$|v_{\mathrm{g}}|$	Infinite-bus voltage amplitude
w_{ml}, $\hat{w}_{nm}$	Weights of autoencoder neural network
$\mathbf{W}_{M \times L}$, $\hat{\mathbf{W}}_{L \times M}$	Matrices of weights in trained neural network
x_1, x_2, x_{tr}	Reactance values of transmission lines and transformers
x_{eq}, x_{f}	Equivalent system reactance and filter reactance
$Y_{\mathrm{Conv}}(s)$	Output admittance of converter
z_m, $\hat{z}_n$	Incoming sum of applied weights and bias
δ, $\bar{\delta}$	Power angle and saturated power angle
δ_{crt}, δ_{pf}	Critical power angle and post-fault power angle
ΔP	Change in active power
ΔT_{sag}	Voltage sag duration
ΔV	Additional internal-voltage
ΔV_{sag}	Voltage sag severity
$\Delta\theta$	Change in voltage phase angle
$\varepsilon_{\mathrm{bc}}$	Added active power error from back-calculation method
ε_{p}, $\bar{\varepsilon}_{\mathrm{p}}$	Actual and modified active-power error
ζ	Damping ratio
θ_{a}, θ_{b}, θ_{c}	Phase angles of converter phase voltages
θ_{g}	Phase angle of infinite bus voltage
θ_{ref}	Reference phase angle
$\sigma(z)$	Sigmoid function
ω_0	Fundamental grid frequency
ω_{d}	High-pass filter bandwidth
ω_{anti}, ω_{res}	Anti-resonance and resonance frequencies
ω_{crt}, ω_{N}	Critical frequency and Nyquist frequency
$\nabla_b, \nabla_{\hat{b}}$, ∇_W, $\nabla_{\hat{W}}$	Partial derivatives for gradient descent equations

1. Introduction

This chapter presents the background of the study, followed by the research objectives and the thesis structure.

1.1 Background

The energy paradigm has made a major shift away from fossil fuels and toward clean renewable energy over the past few decades. The roadmap for renewable energy adoption continues to expand, with more and more converter-based generation (CBG) being integrated into the AC grid. Traditional power grids dominated by synchronous generators (SGs) are evolving into distributed generation systems. Thus, the dynamic behavior of modern power systems differs from SG-dominated systems [1, 2]. CBG exhibits fast and complex transient dynamics under disturbance and fault conditions [3, 4]. On the other hand, the high penetration of CBG has a significant impact on how the power grid is supported during transients and faults [5]. This increases the risk of synchronization instability in the event of grid faults under weak grid conditions [6, 7]. In recent years, grid-forming (GFM) converters have been recognized as a viable solution for power grids with high CBG penetration [8].

Implementing grid-forming control mainly implies recreating the essential properties of SGs [1]. In this context, a number of control schemes have been proposed, among which the P–F and Q–V droop schemes are the most straightforward [7, 9]. Droop control replicates the behaviour of SGs on frequency and voltage regulation [9]. As active power increases, the frequency is decreased, and similarly, as reactive power increases, the voltage amplitude is decreased. These principles have been used in power synchronization control (PSC) for converters connected to weak grids [9]. Moreover, PSC enables the grid converters with maximum power transfer capability in very weak AC grids [10]. By directly adjusting voltage and frequency based on the output power, GFM converters can improve system stability and AC network resilience [11, 12]. Therefore, there is growing

interest in understanding and enhancing the transient stability of GFM converters.

The transient stability of GFM converters refers to the ability to maintain synchronism with the power grid under transient or disturbance conditions [7, 9]. Transmission line faults, large swings in energy production or loads, and frequency fluctuations can all lead to system disturbances and transients [13–15]. The transient stability of GFM converters can be evaluated using numerical-simulation techniques such as phase-plane analysis, steady-state network analysis, and quasi-static large-signal analysis [16–18]. As well, equivalent circuit models can be established for GFM converters with power-synchronization mechanisms to provide physical insight into the control loops [19]. Simplification of models is usually justified only for capturing dynamics after a fault has been cleared, or after a recovery stage has been completed [20, 21]. However, simplified models may not be able to predict actual fault behaviour. For this reason, electromagnetic transient (EMT) studies and the incorporation of higher-fidelity models can be helpful in predicting the transient response of GFM converters. Furthermore, to ascertain transient performance from simulations, it is critical to look beyond limited weak-grid conditions and consider a wide range of grid dynamics as well as assess the LVRT capability of converters by grid codes [22, 23]. Also, applying more advanced analytical and numerical methods such as deep learning, machine learning, and neural networks can help achieve this goal.

With machine learning, complex systems can be described from observational data rather than through first-principles modelling. A machine learning algorithm consists of extracting information from large datasets to build a model that can fit the data most accurately. A deep learning algorithm that is powered by optimization can be used to make predictions and extract features [24]. First, a comprehensive and appropriate set of data needs to be acquired. Then, by handling the data, specifying a cost function, and training deep neural networks, dynamical systems can be characterized. Deep neural networks such as multilayer perceptrons (MLPs) and recurrent neural networks (RNNs) can be designed to better handle sequential information of grid-converter system dynamics [25]. Furthermore, singular value decomposition (SVD), principal component analysis (PCA), and t-distributed stochastic neighbour embedding (t-SNE) are well-suited statistical methods for embedding and visualizing high-dimensional data of nonlinear systems [26]. Deep neural networks are employed in power engineering applications to determine highly nonlinear boundaries between classes and regions [25, 26]. For instance, stacked autoencoders are used for predicting wind and solar photovoltaic power fluctuations, and fault diagnosis [27–29]. Long short-term memory (LSTM) neural networks are also used to model the sequential behaviour of time-dependent power system measurements [28–30]. By integrating machine learning techniques,

spatial characteristics of measurements are transformed into temporal features [31]. Spatiotemporal problems such as renewable energy forecasting, transient stability analysis, and fault detection can be solved by these methods [31]. In addition, to analyse grid-converter system dynamics, time-series forecasting provides a way of predicting future target variables based on learning from past observations. Through time-series forecasting, the converter control system can avoid losing synchronism with the grid by adapting to the grid condition.

On the other hand, as CBGs are integrated into power systems, they can cause harmonic instability in various frequency ranges as a result of their frequency-coupling dynamics [32]. It has therefore become increasingly important to identify the causes of abnormal harmonics and resonances in modern power systems [33]. According to, the small-signal dynamics of converters are capable of inducing negative damping into the power system, depending on the converter's particular controllers and power grid conditions [34, 35]. The time delay in the converter's digital sampling, pulse-width modulation (PWM) and control system causes a negative damping effect, especially at high frequencies [33, 36]. Also, the synchronization loop of converters may result in negative damping at low frequencies [32]. When compared with strong power grids, weak power grids pose additional challenges to harmonic stability. Harmonic instability and new resonance frequencies are more likely to occur in weak grids due to the interaction between passive elements and power electronic converters. Using the dynamic model of the grid-following (GFL) converter, harmonic stability analysis has been conducted for high-voltage direct current (HVDC) systems and grid-connected converters with LCL filters [32–36]. Thus, developing a model that incorporates the specific dynamics of the GFM control and the weak grid would be beneficial for studying the harmonic stability in grid-converter systems.

1.2 Objective and Outline of the Thesis

The primary objective of this thesis is to develop machine learning methods applicable to enhancing the transient stability of GFM converters in weak power grids. Among GFM control methods, PSC will receive special attention due to its desirable properties for weak grid conditions, as discussed in the previous section. More specifically, the objectives of this thesis are:

- To study the synchronization dynamics of the grid-converter system and the deteriorating influence of the reactive power control loop on the transient stability of PSC in weak grids.

- To employ machine learning methods for identifying the transient instability of the grid-converter system and forecasting the voltage

Table 1.1. The main topics covered in each publication.

Main topic	P. I	P. II	P. III	P. IV	P. V	P. VI	P. VII
Transient stability	✓	✓	✓				
Deep learning	✓	✓					
Harmonic stability				✓			
Ancillary services		✓			✓	✓	✓

trajectory during disturbances and faults.

- To propose modified PSC methods with integrated deep neural networks, that provide enhanced transient stability against grid faults and disturbances.

- To establish necessary criteria for improving harmonic stability and LVRT capability in PSC-based grid-connected converters.

This thesis consists of an overview and seven publications. Table 1.1 summarises the main topics covered in the publications. The overview is organized as follows. Chapter 2 presents analytical models, grid-converter control principles, and the thesis preliminaries. Chapter 3 presents an overview of the developed control methods and the stability analyses presented in the publications. A laboratory test setup prepared for experimental evaluation of the proposed control methods is presented in Chapter 4. The summaries of the publications and the scientific contributions are presented in Chapter 5. Finally, Chapter 6 concludes the thesis and discusses the future outlook.

2. Principles of Modeling and Control

The purpose of this chapter is to give a brief overview of modelling and controlling the grid-converter system. This chapter covers voltage-source converters (VSCs), space vectors, and the PSC control method. Additionally, the modelling of electric grids is discussed.

2.1 Three-Phase Systems

A three-phase system is formed by a set of three voltage or current quantities, oscillating with the angular frequency ω_0 and ideally separated in phase angle by $2\pi/3$ rad. A standard three-phase three-wire grid converter system is considered in this thesis. The three phases are denoted as a, b, and c, and the peak values of the three components are equal. In the three-wire system, there is no path for zero-sequence current to flow, so the zero-sequence components are disregarded. A three-phase voltage system can be written as

$$
\begin{aligned}
v_\mathrm{a}(t) &= \hat{V}\cos(\omega_0 t + \theta) \\
v_\mathrm{b}(t) &= \hat{V}\cos(\omega_0 t - 2\pi/3 + \theta) \\
v_\mathrm{c}(t) &= \hat{V}\cos(\omega_0 t - 4\pi/3 + \theta)
\end{aligned}
\tag{2.1}
$$

where $v_\mathrm{a}(t)$, $v_\mathrm{b}(t)$, and $v_\mathrm{c}(t)$ denote the instantaneous phase voltages, $\hat{V}$ denotes the peak value of the phase voltage, ω_0 is the fundamental grid angular frequency, and θ is the phase angle relative to the phase reference. The system of the three-phase voltages can be described as an equivalent two-phase system with two perpendicular axes, denoted with the subscripts α and β. In a complex plane, these axes correspond to the real and imaginary axes, allowing a complex-valued representation of the system. Three-phase-to-two-phase transformation in a stationary reference frame, also called Clarke transformation, generates a complex-valued space vector $\mathbf{v}^s(t)$ as

$$
\mathbf{v}^s(t) = v_\alpha(t) + jv_\beta(t) = \frac{2}{3}K\left[v_\mathrm{a}(t) + e^{j2\pi/3}v_\mathrm{b}(t) + e^{j4\pi/3}v_\mathrm{c}(t)\right]
\tag{2.2}
$$

where K is the space-vector scaling constant. In this thesis, power-invariant scaling is applied by selecting $K = \sqrt{3/2}$. The voltage space vector $\mathbf{v}^s$ can be transformed to a synchronous reference frame (SRF) using the Park transformation as

$$\mathbf{v} = v_\mathrm{d} + jv_\mathrm{q} = e^{-j\theta_\mathrm{g}}\mathbf{v}^s \tag{2.3}$$

where θ_g is the angle of the SRF relative to the stationary reference frame. Transformation into SRF eliminates the rotation of the space vector. Since the rotation of the space vector is removed, its components v_d and v_q will be constant in the steady state. Due to this fact, the dq transformation can be used for both analysing and controlling three-phase VSCs. In this thesis, complex space vectors are used to model the grid-converter system. Complex space vectors are denoted using boldface lower-case symbols.

2.2 Grid-Converter System

Voltage-source converters (VSCs) are power electronic devices composed of semiconductor switches and auxiliary components, such as capacitors, inductors, and transformers [37]. Essentially, the main function of a VSC is to facilitate energy conversion between two (or more) subsystems according to predetermined specifications. The VSC offers the benefit of generating AC voltages without the dependency on the power grid voltage, providing the flexibility of independent control over active and reactive power as well as black start capability.

The VSC consists of a power circuit and a control system. The link between the two is through switching signals and feedback control signals. The power circuit is typically realized using power switches and passive components [38]. A three-phase VSC can be realized based on a variety of configurations. In this thesis, the two-level VSC is considered as the main configuration.

A two-level VSC uses a regulated DC-bus voltage, made by capacitors, to generate controlled voltages at the AC terminals. The circuit diagram of a three-phase two-level VSC with insulated-gate bipolar transistors (IGBTs), together with the DC-bus capacitor and antiparallel-connected diodes is depicted in Fig. 2.1. Antiparallel diodes allow power to flow in
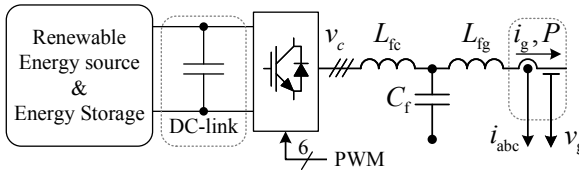

Figure 2.1. Voltage-source converter with an LCL-filter.

both directions. The AC-bus voltage of the converter is generated using pulse-width modulation (PWM). In this thesis, symmetrical suboscillation PWM with the double-update method is used. At every sampling period T_s, the control system computes a set of duty ratios and generates modulating signals m_a, m_b, and m_c. For the design and analysis of the grid-converter control system, switching-cycle-averaged models are applied. The switched model accurately describes the steady-state and dynamic behavior of the converter. Using the averaged model of an ideal two-level VSC, the AC-side terminal voltages can be expressed by

$$\mathbf{v}_\mathrm{c}^\mathrm{s} = \frac{U_\mathrm{DC}}{\sqrt{6}} \left[m_\mathrm{a}(t) + e^{j2\pi/3} m_\mathrm{b}(t) + e^{j4\pi/3} m_\mathrm{c}(t) \right] \tag{2.4}$$

where $m_\mathrm{abc}(t)$ constitute a balanced three-phase modulating signal delivered by a closed-loop control scheme.

The PWM in VSCs causes harmonic current injection into the grid, which must be attenuated to comply with the grid codes and standards such as IEEE Std. 519-2014. Two types of line filters are commonly used in VSCs: L-filters and LCL-filters. L-filters are first-order filters made by using a series inductor in each phase. For a reasonable L-filter size, the switching frequency must be high to sufficiently attenuate harmonics caused by the PWM. The LCL-filter is constructed by connecting capacitors to the inductors using a delta or a wye connection. As compared to the L-filter, the LCL-filter has two main advantages. The LCL-filter suppresses harmonics by 60 dB/dec attenuation above the resonance frequency, rather than 20 dB/dec attenuation as with an L-filter [39]. In this way, even at low and moderate PWM frequencies, sinusoidal line currents are achievable.

In addition, the LCL-filter possesses the advantage of lower total inductance if compared with the L-filter at high switching frequencies. Compared to the L-filter, the LCL-filter provides a faster transient response for VSC since the DC voltage for applying current steps is proportional to the total inductance of the filter [39]. However, the harmonic stability of the grid-converter system is affected by the resonance frequency of the LCL-filter, which is discussed in Publication IV. Mostly, the LCL-filter is considered and discussed in the publications of this thesis.

The LCL-filter (as shown in Fig. 2.1) is modelled by neglecting the resistive parts of the passive elements. Thus, the input-output relations of the LCL-filter, presented in Publication IV, can be modelled by the two admittances $Y_1(s)$ and $Y_2(s)$ defined as

$$Y_1(s) = \left. \frac{i_\mathrm{g}}{v_\mathrm{c}} \right|_{v_\mathrm{g}=0} = \frac{1}{s(s^2 C_\mathrm{f} L_\mathrm{fc} L_\mathrm{fg} + L_\mathrm{fc} + L_\mathrm{fg})} \tag{2.5}$$

$$Y_2(s) = \left. \frac{-i_\mathrm{g}}{v_\mathrm{g}} \right|_{v_\mathrm{c}=0} = \frac{s^2 C_\mathrm{f} L_\mathrm{fc} + 1}{s(s^2 C_\mathrm{f} L_\mathrm{fc} L_\mathrm{fg} + L_\mathrm{fc} + L_\mathrm{fg})} \tag{2.6}$$

where v_c, v_g, and i_g denote the converter-side voltage, grid-side voltage and grid-side current, respectively. L_fc, C_f, and L_fg denote the LCL-filter parameters.

The weak power grid can be modelled equivalently by a three-phase voltage source representing an infinite bus, connected in series with a resistive-inductive impedance representing the grid impedance. The VSC delivers power to the infinite bus through a transformer and parallel transmission lines, forming the grid impedance. Characteristics of the grid impedance (such as SCR and X/R values) can be used to model different grid dynamics. Accurate weak grid modelling is complicated due to the time-variant and frequency-dependent nature of the grid impedance. Thus, simplifying assumptions are often made in studying the impact of grid strength on the grid-converter system. An approach widely used in control literature is to ignore the resistive characteristic of the grid impedance. However, in Publication I of this thesis, the resistive component of the impedance is also considered to cover a wide range of grid characteristics.

2.3   Power Synchronization Control

Since modern power systems increasingly rely on converters, GFM control methods for grid-converter systems have been extensively researched and refined. Over the years, many different control methods and principles have been introduced [1]. From the perspective of this thesis, the power synchronization control method is of particular interest for the application of converters in weak power grids coupled using an LCL filter. A block diagram of the PSC scheme is shown in Fig. 2.2, in which the grid voltage and current are measured for the control system.

The control scheme of PSC without virtual inertia emulation is explained thoroughly in [40, 41]. The active power control loop and the synchronization loop of PSC are demonstrated in Fig. 2.2. Synchronization with the grid is accomplished by the power synchronization loop (PSL) as

$$\theta_\mathrm{ref} = K_\mathrm{ip} \int (P_\mathrm{ref} - P_\mathrm{g}) + \omega_0 t \tag{2.7}$$

$$\delta = \theta_\mathrm{ref} - \theta_\mathrm{g} = K_\mathrm{ip} \int (P_\mathrm{ref} - P_\mathrm{g}) \tag{2.8}$$

where θ_ref and K_ip are the resulting phase angle and the integral gain of the synchronization loop, respectively. P_ref is the active power reference, P_g is the calculated active power by measurements at the point of common coupling (PCC), and ω_0 represents the grid frequency. θ_g is the phase angle of the infinite bus voltage. The initial value of θ_g is supposed to be zero, i.e., $\theta_\mathrm{g} = \omega_0 t$. Power angle δ represents the phase angle difference of the PCC voltage and the infinite bus voltage. Contribution of the converter in regu-
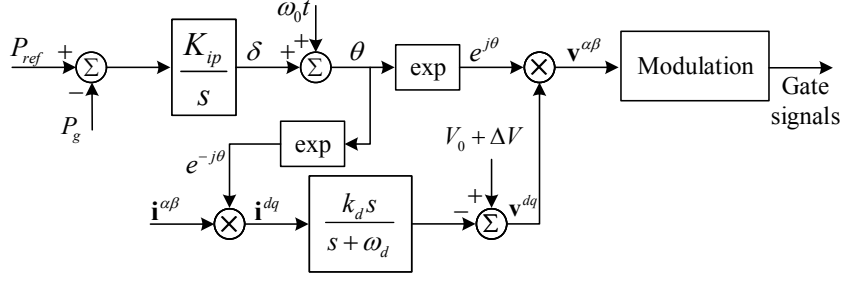
Figure 2.2. Block diagram of PSC.

lating the weak grid voltage and injecting reactive power is accomplished by regulating the internal-voltage delivered by

$$\Delta V = C_{\mathrm{ac}} \left\{ V_{\mathrm{pcc,ref}} - |v_{\mathrm{pcc}}| + C_{\mathrm{Q}}(s) \left[Q_{\mathrm{ref}} - Q \right] \right\} \tag{2.9}$$

where $C_{\mathrm{ac}}(s)$ is the alternating voltage controller and $C_{\mathrm{Q}}(s)$ is the reactive power controller, $V_{\mathrm{pcc,ref}}$ is the voltage-reference for the reactive power control loop, and $|v_{\mathrm{pcc}}|$ is the measured-voltage amplitude at the PCC. The reactive power reference is denoted by Q_{ref} and the measured reactive power is shown by Q. The converter voltage-reference vector $\mathbf{V}_{\mathrm{ref}}^{\mathrm{dq}}$ is generated in synchronous reference frame (SRF) by the following voltage-vector control law to provide active damping of possible resonances

$$\mathbf{V}_{\mathrm{ref}}^{\mathrm{dq}} = (V_0 + \Delta V) - H(s)\mathbf{i}^{\mathrm{dq}} \tag{2.10}$$

$$H(s) = \frac{k_{\mathrm{d}} s}{s + \omega_{\mathrm{d}}} \tag{2.11}$$

where, V_0 is the rated voltage, $\mathbf{i}^{\mathrm{dq}}$ is the current vector of the converter in SRF, and $H(s)$ is a high-pass filter for active damping in which k_{d} and ω_{d} are the gain and bandwidth of the filter, respectively. It should be noted that a backup PLL is included in the synchronization loop for seamless initial synchronization with the grid [40]. Linearized dynamic model describing the relation between the active power increment ΔP following an increment in the power angle $\Delta\theta$ is given by $J_{P\theta(s)}$ as

$$J_{P\theta}(s) = \frac{\Delta P}{\Delta\theta}. \tag{2.12}$$

The transmission zeros of the linearized model $J_{P\theta(s)}$ restrict the realizable bandwidth of the PSC control system. The place of the transmission zeros are depending on the operating point of the converter as explained in [40, 41]. The particular situation in which the zeros reach to the origin is when $\delta = \pm\pi/2$; Thus, sufficient bandwidth and gain cannot be achieved when the operating point of the converter is close to $\delta = \pm\pi/2$.

3. Transient- and Harmonic-Stability of Grid-Converters

The growing integration of CBGs into the power system, besides the demand for transferring power between remote points, requires a stable interconnection of VSCc with weak grids. Weak grids introduce voltage and frequency volatility that require a robust and reliable control of grid-converter systems. The use of CBGs should also contribute to the stabilization of weak power systems. Therefore, this chapter focuses on the transient-stability and harmonic-stability of grid-converter systems.

3.1 Transient Stability

Stability problems are generally divided into two categories: small-signal and large-signal. Small-signal stability is studied by first establishing a steady operating point and then linearizing the non-linear part of the control structure. Having a steady-state operating point is a precondition for the small-signal analysis [42]. However, large-signal disturbances such as grid faults may render the stable operating point unattainable, thereby necessitating a study of large-signal stability. This type of stability analysis, known as large-signal stability, is crucial in understanding the synchronization stability of grid-converter systems. Synchronization stability refers to how well the converter can track and maintain synchronization with the grid during large disturbances. This thesis uses transient stability as a convenient term to describe large-signal synchronization stability.

Specifically, for achieving seamless integration of CBG into weak grids under normal operating condition, PSC presents a viable solution which allows transferring power between remote points of the grid [43]. However, during severe grid disturbances and transients in weak grids, there are fundamental distinctions between a PSC-controlled grid-converter system and a synchronous machine including different transient responses [44]. The programmability of a PSC-controlled grid-converter system significantly affects its transient response. Moreover, the system's fault-ride-through capability can be impacted by its limited short-circuit current. In addition,

the transient stability of PSC-controlled converters during severe grid disturbances in weak grids is vulnerable and substantially different from that of synchronous machines.

Transient stability of GFM control schemes has been extensively discussed in the literature [9,20,22,45–48]. Specifically, the transient stability of GFM converters has been addressed by design-oriented analyses under large-signal disturbances by studying the equilibrium points and phase portraits in [9] and [45]. Similarly, phase portraits have been used for PSC and critical clearing angle has been identified to facilitate the design of power system protection in [46]. The nonlinear characteristics of the synchronization loop are also discussed in [20] where the averaging method is employed to present a time-domain expression during disturbances and to establish the related stability criterion.

However, neglecting the grid dynamics makes these design-oriented analyses inappropriate for studying and enhancing the transient stability of the grid-converter systems [22, 47]. The study in [22] demonstrates that the loss of synchronization following a grid voltage sag is essentially the result of transient interaction of the weak terminal voltage and the converter synchronization loop. In [47], the authors addressed the challenges of paralleled systems that influence the transient stability by considering the dynamics of islanded microgrids. The dynamic synchronization characteristics of grid-tied converters regarding the effect of grid impedance, controller parameters, and current references has been explored in [48] as well. Moreover, the authors in [49] developed models for the transient stability assessment of grid-tied converters exposed to severe grid faults.

In addition to the existing literature, Publications I, II, and III discuss the transient stability of PSC and present developed control methods. Publications I, II, and III are briefly described in the following subsections.

3.1.1 Transient Stability of PSC

In practice, GFM converters are supplied via a DC-link regulated by energy storages to provide supportive services such as power quality improvement and virtual inertia emulation. The DC-link voltage is consequently regulated during grid transients. As demonstrated in Fig. 3.1, the VSC in connected to the grid via an LCL-filter (with equivalent inductance L_{LCL}), a star-delta transformer L_{trans}, and two transmission lines L_{line1} and L_{line2}. The capacitance of the filter and the stray capacitance of the transmission lines have insignificant influence on the transient stability of the converter [46]. Thus, the LCL filter and the two transmission lines are modelled by means of an equivalent inductance for studying the transient stability of the converter. In the supposed control scheme, the converter adjusts the output reactive power to preserve the PCC voltage and support the grid voltage during voltage sags. In this case, the internal voltage of
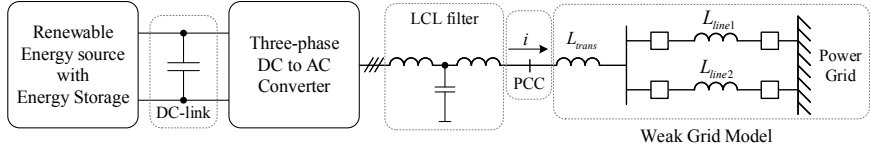
Figure 3.1. Single-line diagram of a grid-connected converter under weak grid operating condition.

the converter is set at the maximum allowed value, determined by the reactive power control loop. Thus, the dynamic response of the PSC synchronization loop can be described by a first-order differential equation as

$$\dot{\delta} = K_{\mathrm{ip}}(P_{\mathrm{ref}} - P_{\mathrm{g}}). \tag{3.1}$$

The equivalent impedance of the filter, transmission lines, and transformer defines the short-circuit ratio (SCR) of the grid. The SCR establishes bounds on the maximum possible transmitted active-power and the PSC transient stability margin which are mainly influenced by the weak-grid operating condition. Weak-grid operating condition imposes a higher power angle than a strong-grid operating condition. Furthermore, the gain and bandwidth of PSC are dependent on the power angle and the operating point of the converter. As the power angle increases, the gain and bandwidth of PSC reduce. Therefore, the transient stability of PSC is dependent on the dynamic response of the power angle.

In Publications I and II, voltage sags with various duration and severity in the grid are considered. The SCR of the grid also covers a range of strong grid, weak grid, and ultra-weak grid. Following a severe voltage sag, the system reaches a new stable equilibrium point if the power angle converges to a new value. This is contingent on the pre-disturbance operating point as well as the SCR value at pre-disturbance, during-voltage-sag, and post-disturbance operation.

3.1.2 Deteriorating Effect of Reactive Power Control Loop

GFM converters support the grid to mitigate the adverse effects of voltage disturbances by supplying reactive power. Thus, the risk of cascaded failure and voltage collapse would be reduced. The reactive power control law introduced by (2.9) is intended to regulate the PCC voltage and supply reactive power within the limits established by grid codes for continuous operation. During a three-phase voltage disturbance, the internal voltage of the converter increases to regulate the PCC voltage as well as supplying reactive power which should be limited to the rated capacity of the converter. To better demonstrate the influence of the reactive power control loop on transient angle stability, the output active power of a PSC-controlled converter with deactivated reactive power control loop and fixed
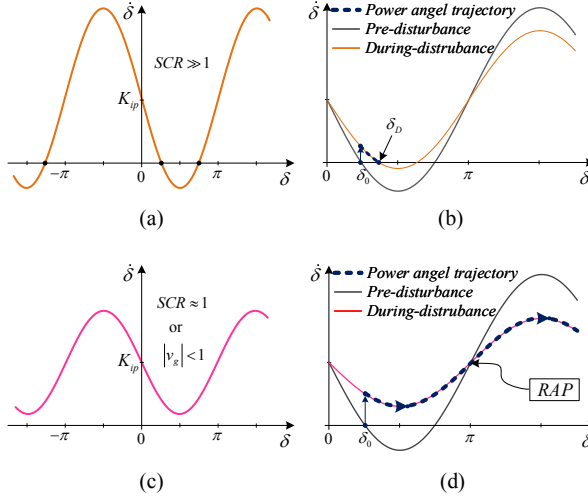
Figure 3.2. Phase-portrait and power angle trajectory (a) phase-portrait of PSC with equilibrium points, (b) power angle trajectory when SCR is greater than one during fault, (c) phase-portrait of PSC without equilibrium points, and (d) power angle trajectory when SCR is close to 1.

internal voltage can be expressed by

$$P_{\mathrm{g}} = \frac{V_0 \, |v_{\mathrm{g}}|}{\omega_0 L_{\mathrm{T}}} \sin(\delta) \qquad (3.2)$$

where $|v_{\mathrm{g}}|$ denotes the infinite bus voltage and L_{T} is the equivalent inductance of the system which is defined by

$$L_{\mathrm{T}} = L_{\mathrm{LCL}} + L_{\mathrm{trans}} + \frac{L_{\mathrm{line1}} \times L_{\mathrm{line2}}}{L_{\mathrm{line1}} + L_{\mathrm{line2}}}. \qquad (3.3)$$

Given the reactive power controller in (2.9), the relationship expressed by (3.2) can be turned into

$$P_{g,Q} = \frac{(V_0 + \Delta V) \, |v_g|}{\omega_0 L_T} \sin(\delta). \qquad (3.4)$$

During a severe voltage sag, the grid voltage dip would lead to an immediate rise in the output reactive power of the converter due to the voltage difference between the converter and the grid. In accordance with the reactive power controller in (2.9), the converter internal voltage would be limited to a certain value less than the rated value to manage the output reactive power by the controller $C_{\mathrm{Q}}(s)$.

Since the reactive power of the converter is limited to its rated value, during a severe voltage sag the converter internal voltage cannot instantly restore to the maximum value. In this case, $\Delta V < 0$ and $P_{\mathrm{g},Q} < P_{\mathrm{g}}$, thus this decrease in the output power will lead to a rise in the acceleration of the power angle during the grid fault, which may result in transient angle instability. This is referred to as the deteriorating influence of
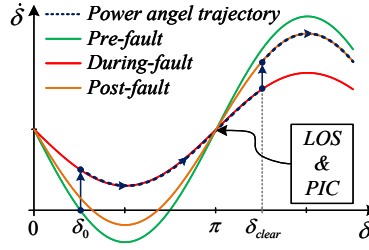
Figure 3.3. Phase portrait of PSC-based grid-converter system following a solid fault.

reactive power controllers on the transient stability of PSC-controlled grid-converter systems. Although the converter internal voltage changes during severe voltage sags and faults, caused by the variation of the power angle, it is bound to a smaller value compared to the nominal value V_0.

By substituting (3.4) into (3.1) and assuming various active power references and operating conditions, two different cases for stability analysis would be assumed. Firstly, a weak grid with an SCR greater than 1 is provided and the system reaches a stable equilibrium point after the disturbance (as shown in Fig. 3.2 (a) and (b)). Secondly, there are no stable equilibrium points or due to the transmission zeros of $J_{P\theta}(s)$, which are located at $\delta = \pm\pi/2$, transient instability takes place (as shown in Fig. 3.2 (c) and (d)). Fig. 3.2 (a) and (c) illustrates the phase portraits of the two discussed stability cases, respectively. Fig. 3.2 (b) and (d) show the power angle trajectory of the converter following severe voltage sags fault for the stable and unstable cases, respectively. As shown in Fig. 3.2 (d), the direction of the active power changes and reverse active power flow (RAP) occurs. This analysis is in accordance with the following presumptions:

- The converter output voltage is adjusted and limited by the reactive power controller to support the grid voltage during the voltage sags.

- The converter can tolerate its contribution to the grid fault current.

- Because of the high-impedance weak grid, the power angle of the converter is large enough to limit the gain and bandwidth of $J_{P\theta}(s)$.

The power angle trajectory of the system shown in Fig. 3.1 is depicted in Fig. 3.3, where the power angle at the instant of fault clearance δ_{clear} is greater than π. The studied system is described in detail in Publication III, where the fault clearance time is set to be equal to five power-system cycle to show the strong possibility of transient instability as well as loss of synchronization (LOS) and power injection collapse (PIC).

Table 3.1. Impedance characteristics of the studied grid-converter system

Parameter	Description	Value
X/R	Reactance to resistance ratio	16, 10, 6, 2, 1.5
SCR	Short circuit ratio	3.5, 3, 2.5, 2, 1.5

3.1.3   Impact of grid dynamics

Grid dynamics are defined by the system's fault current rating (i.e. SCR value) and reactance to resistance ratio of the system (the X/R value) [50]. In Publication I, the typical SCRs and X/R values of weak grids for different voltage levels are considered, as given in Table 3.1.   Under weak grid conditions when the active power capacity is limited by the grid voltage and impedance, the bandwidth of the synchronization loop of PSC decreases rapidly as the converter power angle approaches the critical value of $\pi/2$. In this case, the PSC-controlled converter may become unstable and lose synchronization following a large voltage sag. Based on the severity of the voltage sag, the grid characteristics, and the operating point of the converter, it is possible to detect transient instability in a timely manner by machine learning algorithms. Detailed algorithms are elaborated in Publication I.

3.2   Enhancing Transient Stability of PSC by Back-Calculation Method

This section presents a PSC-based control method with enhanced transient stability (ETS) to avoid LOS and PIC. The ETS-PSC is introduced in Publication III. When the power angle is close to $\pi/2$ (i.e. weak-grid operating condition), the gain and bandwidth of $J_{P\theta}\left(s\right)$ decreases considerably. So, an active power decrease driven by a grid fault causes the control system to rapidly increase the power angle. In this case, the active power reference will remain greater than the measured active power and lead to transient instability. Basically, the system is non-minimum phase and there is no feature in PSC that bounds the power angle. Therefore, as the active power error is the main reason for unbounded increase of the power angle, by introducing power-angle saturation and active-power back-calculation, the active power reference in PSC can be modified leading to enhanced transient stability.

3.2.1 Modified Active Power Error

In normal operating condition, the power angle never reaches $\pi/2$, thus no problem is encountered. However, for large steps in the active-power error due to the grid disturbances, the PSL output signal exceeds critical power-angle δ_{crt}, which is determined based on the lower limits of the bandwidth and gain of the controller. Especially for higher grid impedance and lower post-fault SCR, the power-angle produced by the PSL exceeds the critical power-angle. Therefore, the saturation function, illustrated in Fig. 3.4, limits the PSL power-angle, and the saturated power-angle $\bar{\delta}$ should be used as the reference to the converter voltage-angle. The
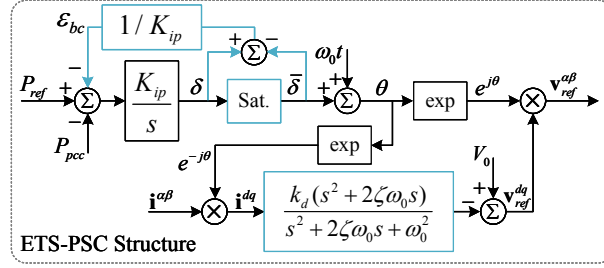

Figure 3.4. Block diagram of ETS-PSC structure.

saturation function is expressed by

$$\bar{\delta} = sat(\delta, \delta_{\mathrm{crt}}) = \begin{cases} \delta_{\mathrm{crt}}, & \delta > \delta_{\mathrm{crt}} \\ \delta, & -\delta_{\mathrm{crt}} \leq \delta \leq \delta_{\mathrm{crt}} \\ -\delta_{\mathrm{crt}}, & \delta < -\delta_{\mathrm{crt}} \end{cases} \tag{3.5}$$

Because of the saturation, the modified PSL contains a nonlinearity and it is important to prevent windup in the PSL. By applying the following back-calculation method, the PSL input is altered from the actual active-power error ε_p to a modified active-power error $\bar{\varepsilon}_p$. The modified PSL can be described as

$$\begin{aligned} \bar{\delta} &= sat(\delta, \delta_{\mathrm{crt}}) \\ \varepsilon_p &= P_{\mathrm{ref}} - P_{\mathrm{pcc}} \\ \varepsilon_{\mathrm{bc}} &= \tfrac{1}{K_{\mathrm{ip}}}(\delta - \bar{\delta}) \\ \delta &= K_{\mathrm{ip}} \int \bar{\varepsilon}_{\mathrm{p}} = K_{\mathrm{ip}} \int \left(\varepsilon_{\mathrm{p}} - \varepsilon_{\mathrm{bc}} \right) \end{aligned} \tag{3.6}$$

where, ε_{bc} represents the effect of the back-calculation method on the modified PSL. In other words, the modified active-power error $\bar{\varepsilon}_p$ is assumed to be such that the saturation operator never is entered and the integrator windup in PSL would not occur. Modifying the active power error by the back-calculation method and calculating the converter voltage-angle θ based on the saturated power-angle reference $\bar{\delta}$, result in the ETS-PSC structure depicted in Fig. 3.4 and the phase portrait shown in Fig. 3.5.

3.2.2   DC Component Suppression

PSC structure has a limited gain for suppressing DC components of the converter current caused by transients in high impedance grids. Thus, following any switching or transient in the grid, DC components decay slowly and occupy the converter current capacity. Since PSC-controlled converter behaves as a three-phase balanced voltage source, the converter contribution in the fault current, during voltage dips on the AC grid, is instantaneous and the converter can deliver the natural instantaneous short-circuit current without delay. Natural instantaneous short-circuit current is the potential current that would be supplied without any current limitation. The natural fault current consists of a steady-state AC component and a decaying DC component. Although the grid impedance may be more resistive in low-voltage microgrids, basically the grid impedance and the converter output filter are highly inductive. Consequently, the natural time constant of the decaying DC component is high enough to cause thermal and overcurrent issues during transients. In publication III, to suppress the DC components of the converter and improve fault-ride-through capability of PSC, the high-pass filter $H(s)$ in the PSC structure is replaced by $H_{\mathrm{ETS}}(s)$ defined as

$$H_{\mathrm{ETS}}(s) = \frac{k_{\mathrm{d}}(s^2 + 2\zeta\omega_0 s)}{s^2 + 2\zeta\omega_0 s + \omega_0^2} \tag{3.7}$$

where ζ determines the suppression capability of the DC components in ETS-PSC. The introduced $H_{\mathrm{ETS}}(s)$ provides both damping and DC component suppression. More details are presented in Publication III.

3.3   Enhancing Transient Stability of PSC by LSTM Neural Networks

The PSC method performs poorly when a phase shift occurs in the grid voltage. Additionally, the GFM control methods should also satisfy the LVRT requirements. Forecasting grid voltage trajectory can be useful to prevent the loss of synchronization in PSC due to the variety of operating
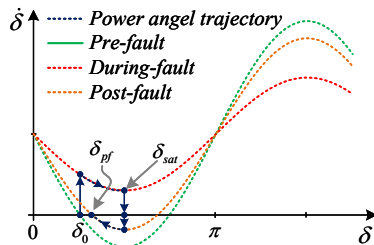

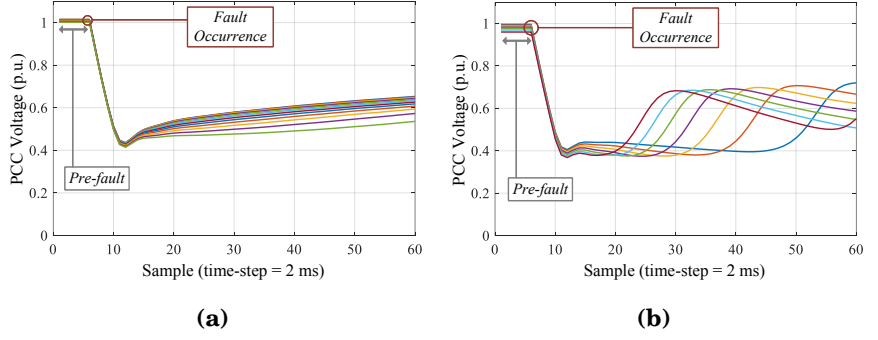**Figure 3.5.** Phase portrait of ETS-PSC following a solid grid fault.

Figure 3.6. PCC voltage trajectory during faults in a weak grid (a) stable operation of the converter during voltage sag, and (b) transient instability in the converter and loss of synchronization with the grid.

conditions and grid faults. This is due to the voltage volatility of weak grids. The purpose of this section is to demonstrate how LSTM neural networks were employed to process PCC voltage trajectory during transients by exploiting their features. The LSTM neural network is adopted in Publication II to predict the behaviour of the grid voltage and adapt the active power reference and internal voltage reference of the converter for both satisfying the LVRT requirements of the grid and improving the transient stability of PSC.

3.3.1 PCC Voltage Trajectory During Grid Faults

Following a fault event in the grid, the PCC voltage drops. During the very first moments, the control system of the converter attempts to keep up the PCC voltage by increasing the internal voltage of the converter. If there is a substantial reduction in the grid voltage, the converter may no longer maintain synchronization with the grid. The trajectory of PCC voltage is illustrated in Fig. 3.6 for two different fault events. The case that the converter remains stable during fault is demonstrated in Fig. 3.6(a) for a couple of pre-fault operating conditions. In this case, the converter delivers reactive power to support the grid without affecting grid synchronization and helps restore voltage. In a more severe voltage sag, although the converter attempts to increase the internal voltage and support the grid voltage, due to the loss of synchronization, the converter becomes unstable and the PCC voltage starts fluctuating as depicted in Fig. 3.6(b).

As shown in Fig. 3.6, the stable operation of the converter during grid faults is contingent on the severity of the voltage drop and the pre-fault operating point of the converter which is a function of the grid impedance as well. By extracting the pattern of the PCC voltage trajectory, it would be possible to process and predict the transient stability of the grid-converter system following a grid fault. The trajectory of the PCC voltage after a

fault reveals whether the converter can support the grid voltage without loss of synchronization.

Following the voltage sag, if the voltage begins to recover, it indicates that the converter will be successful in maintaining the grid voltage and operating smoothly. On the other hand, if the voltage recovery fails after the voltage drop, the converter will collapse and lose synchronization.

3.3.2   Forecasting PCC Voltage Trajectory by LSTM

To forecast the PCC voltage trajectory, LSTM neural network provides straightforward processing of order among samples of a sequence. Among neural networks, LSTM architecture introduces inherent advantages for handling sequences and time series. LSTM learns to map the inputs over time to output and captures the dependencies of observations with large time step distances. This capability of learning the order of the data is not offered by multilayer perceptron (MLP) or convolutional neural networks (CNN) [51, 52]. Additionally, LSTM can be used for time-series prediction using time-window techniques, and naturally detects the temporal dependence from input observations. Thus, the most prominent context of the PCC voltage samples to the expected output (i.e. PCC voltage trajectory) would be extracted and can be modified dynamically to continue the given sequence. In Fig. 3.7, the proposed LSTM network in Publication II with deep architecture and multiple hidden layers is depicted.

The input data of the employed LSTM network are samples of the PCC voltage at the current time step $\mathbf{V}_t$ and the hidden state of the preceding time step $\mathbf{H}_{t-1}$, as shown in Fig. 3.7. The concatenated data of $\mathbf{V}_t$ and $\mathbf{H}_{t-1}$ are processed by three fully connected (FC) layers including input gate, forget gate, and output gate. Each FC layer has an activation function with the type of sigmoid σ or hyperbolic tangent $\tanh$ to compute the
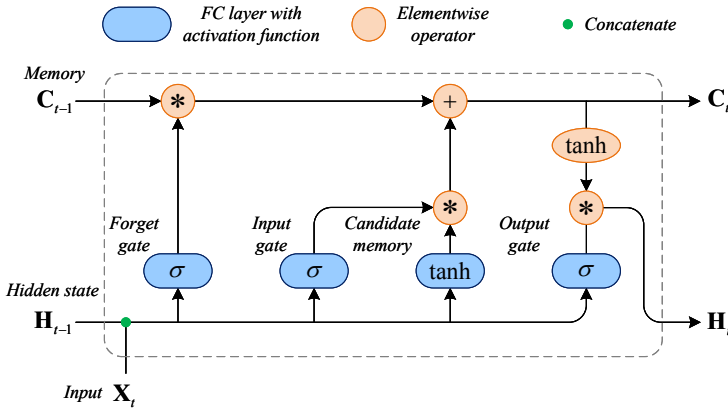

Figure 3.7. Architecture of a cell in an LSTM network.

values of the subsequent gates. The sigmoid activation function maps the values of the input gate, forget gate, and output gate to the range of $(0, 1)$. The number of hidden units is h and the batch size is k. By assuming that the number of inputs is l, the input at the current time step would be $\mathbf{V}_t \in \Re^{k \times l}$. Thus, the hidden state of the preceding time step is $\mathbf{H}_{t-1} \in \Re^{k \times h}$. Similarly, the gates at the current time step t can be defined as the input gate $\mathbf{I}_t \in \Re^{k \times h}$, the forget gate $\mathbf{F}_t \in \Re^{k \times h}$, and the output gate $\mathbf{O}_t \in \Re^{k \times h}$ given by

$$
\begin{aligned}
\mathbf{I}_t &= \sigma\left(\mathbf{V}_t \mathbf{W}_{\mathrm{vi}} + \mathbf{H}_{t-1} \mathbf{W}_{\mathrm{hi}} + \mathbf{b}_{\mathrm{i}}\right) \\
\mathbf{F}_t &= \sigma\left(\mathbf{V}_t \mathbf{W}_{\mathrm{vf}} + \mathbf{H}_{t-1} \mathbf{W}_{\mathrm{hf}} + \mathbf{b}_{\mathrm{f}}\right) \\
\mathbf{O}_t &= \sigma\left(\mathbf{V}_t \mathbf{W}_{\mathrm{vo}} + \mathbf{H}_{t-1} \mathbf{W}_{\mathrm{ho}} + \mathbf{b}_{\mathrm{o}}\right)
\end{aligned}
\tag{3.8}
$$

where $\mathbf{W}_{\mathrm{vi}}, \mathbf{W}_{\mathrm{vf}}, \mathbf{W}_{\mathrm{vo}} \in \Re^{l \times h}$ and $\mathbf{W}_{\mathrm{hi}}, \mathbf{W}_{\mathrm{hf}}, \mathbf{W}_{\mathrm{ho}} \in \Re^{h \times h}$ are the weight parameters for the input, forget, and output gates, respectively. The bias parameters are denoted by $\mathbf{b}_{\mathrm{i}}, \mathbf{b}_{\mathrm{f}}, \mathbf{b}_{\mathrm{o}} \in \Re^{1 \times h}$ for the input, forget, and output gates, respectively. Prospect memory cell $\mathbf{P}_t$ is the other element of LSTM computed by $\tanh$ resulting a value in the range of $(-1, 1)$ at the time step t as

$$
\mathbf{P}_t = \tanh\left(\mathbf{V}_t \mathbf{W}_{\mathrm{vp}} + \mathbf{H}_{t-1} \mathbf{W}_{\mathrm{hp}} + \mathbf{b}_{\mathrm{p}}\right)
\tag{3.9}
$$

where $\mathbf{W}_{\mathrm{vp}} \in \Re^{l \times h}$ and $\mathbf{W}_{\mathrm{hp}} \in \Re^{h \times h}$ are weight parameters and $\mathbf{b}_{\mathrm{c}} \in \Re^{1 \times h}$ is a bias parameter for computing the prospect memory cell $\mathbf{P}_t$ at the current time step. In LSTM there are two dedicated gates for governing input and forgetting purposes. The input gate $\mathbf{I}_t$ determines how much of the new data should be taken into account by means of $\mathbf{P}_t$. The forget gate $\mathbf{F}_t$ addresses what portion of the preceding memory cell content $\mathbf{M}_{t-1} \in \Re^{k \times h}$ should be retrained. Correspondingly, the memory cell $\mathbf{M}_t$ can be defined by

$$
\mathbf{M}_t = \mathbf{F}_t * \mathbf{M}_{t-1} + \mathbf{I}_t * \mathbf{P}_t.
\tag{3.10}
$$

The hidden state $\mathbf{H}_t \in \Re^{k \times h}$ in LSTM is considered as a gated type of the memory cell content $\mathbf{M}_t$ with an activation function $\tanh$ as

$$
\mathbf{H}_t = \mathbf{O}_t * \tanh(\mathbf{M}_t)
\tag{3.11}
$$

thereby, the values of $\mathbf{H}_t$ are all in the range of $(-1, 1)$.

3.3.3 Training, Evaluation, and Application

A large number of contingencies simulated in MATLAB/Simulink have been used for training the LSTM network presented in Publication II. The training data consists of various pre-fault operating conditions, a wide range of SCR values, and a large collection of short-circuit fault impedances. Three-phase to-ground faults at various locations were simulated and the trajectory of PCC voltage and stability condition of the converter were
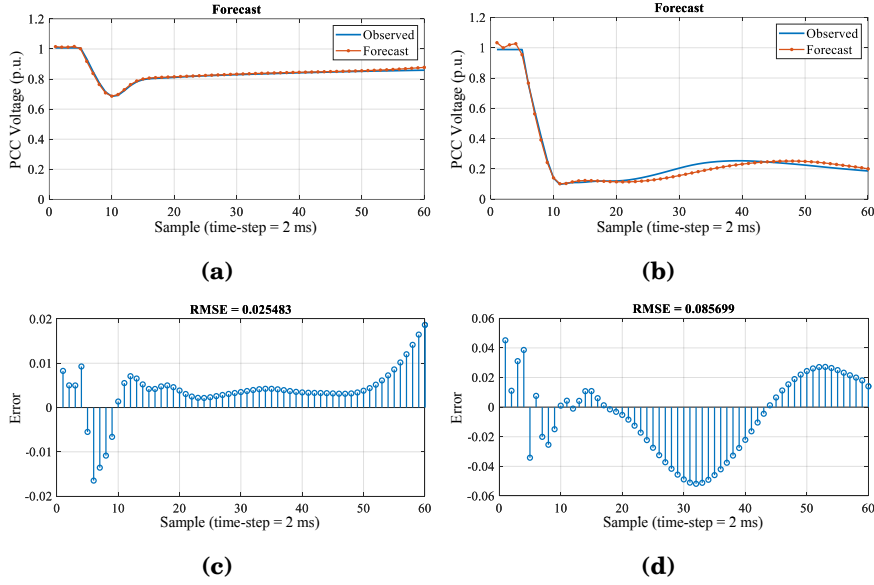
Figure 3.8. Comparison of the sampled PCC voltage and the LSTM forecast (a) PCC voltage trajectory during stable operation of the converter, (b) PCC voltage trajectory during loss of synchronization in the system, (c) forecast error of the LSTM network for the former case, and (d) forecast error for the latter case.

logged. It was assumed that the short-circuit faults could be cleared after five cycles by disconnecting the faulted line. This resulted in 25000 simulation cases where 37% of the logged data are related to the case where the loss of synchronization happens (as presented in Publication II). From the recorded data, 75% of stable cases and 75% of unstable cases were randomly dedicated to training the network. The remaining 25% of the recorded data were used for the evaluation of the trained network. The PCC voltage samples were collected at a sampling period $T_s = 2$ ms during a time interval including pre-fault and during-fault operation of the converter. Consequently, a proper dataset was generated to train the LSTM network for achieving an accurate voltage trajectory extraction and prediction.

To evaluate the prediction accuracy of the trained LSTM, the root mean squared normalized error (RMSE) is considered as the performance index. Sampled PCC voltages and the output of the trained LSTM for two different cases are shown in Fig. 3.8. First, the case that the converter continues operation without loss of synchronization after the fault occurs as shown in Fig. 3.8(a). Second, the case that the converter loses synchronization and becomes unstable after the grid fault as shown in Fig. 3.8(b). The accuracy of the trained LSTM network is illustrated in Fig. 3.8(c) and (d) by calculating the RMSE value of each voltage trajectory forecast. The calculated RMSE reveals that the trained LSTM can extract and predict

Table 3.2. Specifications of the trained LSTM network

Parameter	Description	Value
l	Number of inputs (look back samples)	10
h	Number of hidden layers	75
k	Batch size	25
Epochs	Number of epochs	500
RMSE	Normalized RMSE of network training	0.021468

the PCC voltage trajectory regardless of uncertainty existing in data and missing values of data points. The proposed LSTM network is trained offline by the generated data coming from time-domain simulations for various grid conditions and grid faults. Specifications of the trained LSTM network are summarized in Table 3.2.

3.3.4   LSTM-Integrated PSC

During grid faults, both LVRT requirements and stable operation of the converters should be achieved. By extracting and predicting the PCC voltage trajectory, presented in Publication II, new references for the delivered active power and the internal voltage of the converter can be calculated. The LSTM network processes the PCC voltage samples and generates the PCC voltage trajectory v_{LSTM}. Thus, the predicted converter current I_{C} can be expressed by

$$I_{\mathrm{C}} = \frac{V_0 - V_{\mathrm{pcc}}\angle\theta_{\mathrm{pcc}}}{x_{\mathrm{f}}} \tag{3.12}$$

where, V_{pcc} and θ_{pcc} are the amplitude and angle of the PCC voltage, respectively. The impedance of the converter output filter x_{f} is small enough to assume that the phase difference between the internal voltage of the converter and the voltage of PCC is negligible ($\alpha \approx 0$). Assuming that the required internal voltage of the converter during grid faults is V_{ad} and the rated current of the converter is $I_{\mathrm{C}}^{\mathrm{rated}}$, V_{ad} can be expressed by

$$V_{\mathrm{ad}} \approx x_{\mathrm{f}}I_{\mathrm{C}}^{\mathrm{rated}} + v_{\mathrm{LSMT}}. \tag{3.13}$$

Next, by considering the LVRT requirements (discussed in [53] for power-angle synchronization control) and the capacity of the converter, new reference signals for PSC can be calculated dynamically as

$$V_{\mathrm{ad}} = \begin{cases} V_0 & v_{\mathrm{LSMT}} > 0.9 \\ x_{\mathrm{f}}I_{\mathrm{C}}^{\mathrm{rated}} + v_{\mathrm{LSMT}} & v_{\mathrm{LSTM}} < 0.9 \end{cases} \tag{3.14}$$

$$P_{\mathrm{ad}} = \begin{cases} V_0 & v_{\mathrm{LSMT}} > 0.9 \\ \min\{P_{\mathrm{ref}}, P_{\mathrm{LVRT}}\} & v_{\mathrm{LSTM}} < 0.9 \end{cases} \tag{3.15}$$

Transient- and Harmonic-Stability of Grid-Converters

where, P_{ad} and P_{ref} are the grid-fault-adapted and pre-fault active power reference for PSC, respectively; and P_{LVRT} is the maximum allowed active power reference in accordance with the LVRT requirements. The modified control system is demonstrated in Fig. 3.9 and the performance of the developed control method is discussed in Publication II.
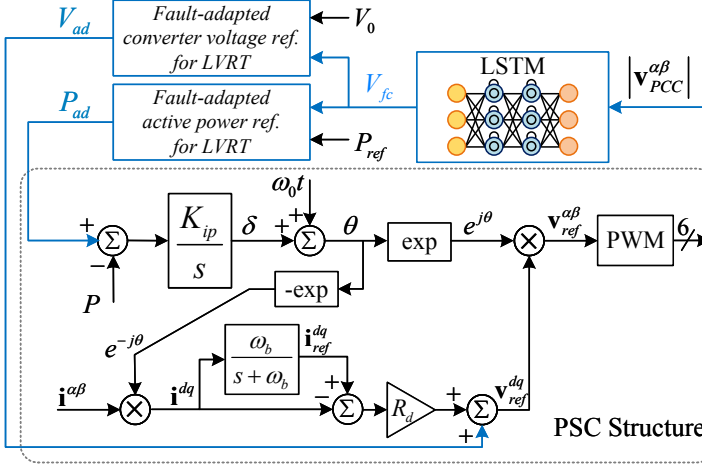

Figure 3.9. LSTM-integrated PSC.

3.4 Enhancing Transient Stability of PSC by Deep Learning Methods

The objective of this section is to improve the performance and accuracy of early instability detection of PSC by utilizing deep learning methods. Deep learning methods are highly dependent on the representation of the data they are given. The performance of learned representations is often much better than that of unlearned representations. The learned representation could then be used to detect early PSC instability due to grid voltage sags.

3.4.1 Representation Learning and Feature Selection

Publication I proposes a method that uses the measurements of the PCC voltage trajectory taken before and during a fault. Creating a proper dataset for training deep-learning-based classifiers is the key to assessing transient stability. Table 3.3 lists a large number of operating points, grid conditions, and disturbance types (i.e. disturbance duration and disturbance severity) included in the generated dataset. By extracting patterns from raw data based on a proper representation, classification becomes fast and accurate. A structured and intelligently indexed collection of data can significantly speed up operations. A description is provided below on designing the right set of features, determining the PCC voltage, and

24

Table 3.3. Specifications of the Generated Data for Training and Validation of the Neural Networks

Parameter	Description	Value
P_{ref}	Pre-fault active power	0.05 : 0.05 : 1 p.u.
ΔV_{sag}	Voltage sag severity	0.10 : 0.05 : 0.85 p.u.
ΔT_{sag}	Voltage sag duration	30 : 10 : 120 ms
X/R	X/R ratio	16, 10, 6, 2, 1.5
SCR	Short circuit ratio	3.5, 3, 2.5, 2, 1.5
N_{Total}	Total combinations	80000
N_{Sta}	Stable cases	58528
N_{Ins}	Unstable cases	21472
N_{Tr}	Cases for training	32208
N_{Val}	Cases for validation	10736
T_w	Sampling window	40 ms
T_s	Sampling period	1 ms

collecting the data. Since the converter stability depends on the pre-fault operating point, the voltage sag severity, the duration of the voltage sag, and the characteristics of the grid (i.e. SCR and X/R values), the extracted points should represent these features influencing the converter stability. To illustrate the effects of these five factors on the transient stability of PSC, measurements of the PCC voltage regarding stable and unstable cases are shown in Fig. 3.10(a) and (b), respectively. The pre-fault voltage magnitude represents the pre-fault operating condition, which can be taken as an indication of the pre-fault active- and reactive power of the converter and the pre-fault power angle. Converter dynamics and transient stability are affected by the pre-fault power angle. Furthermore, the voltage drop is directly related to fault location and fault impedance. Therefore, PCC voltage just after a fault is a reliable indicator of disturbance severity, another major determinant of transient instability. Prior to the fault clearance, the voltage trajectory can be used as an indicator of the converter's ability to restore the PCC voltage by injecting reactive power, as well as its stability. Also, the sampling window is selected large enough to encompass the time constant of the synchronization loop of PSC and small enough to provide early transient instability detection. Consequently, machine learning classifiers can accurately predict converter transient stability status based on the PCC voltage trajectory. Data specifications for training neural networks are listed in Table 3.3.

In Publication I, a representation learning algorithm known as autoencoder is applied to the original data which consists of an encoder function and a decoder function. The encoder converts the input data into a learned representation, whereas the decoder converts the learned representation
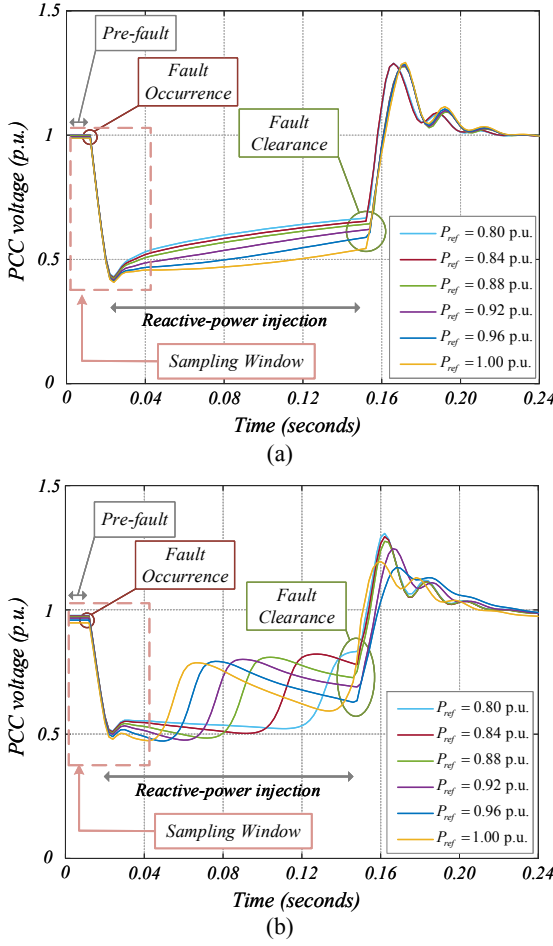
Figure 3.10. The PCC voltage during severe voltage sags regarding transient stability of the converter, (a) stable synchronization during a 55% voltage sag when $SCR = 2.5$ and $P_{ref} = 0.8 : 0.04 : 1$ p.u., and (b) unstable synchronization with the grid during a 50% voltage sag when $SCR = 1.5$ and $P_{ref} = 0.8 : 0.04 : 1$ p.u..

back into the original representation. The autoencoder is trained to preserve the most important information and make the new representation robust to noise and corrupted data. Figure 3.11 illustrates the denoising autoencoder used in Publication I.

The autoencoder is a neural network with one hidden layer and trained to reconstruct the original representation with as little error as possible. The autoencoder network consists of an encoder $\mathbf{h} = f(\mathbf{v})$ and a decoder $\hat{\mathbf{v}} = g(\mathbf{h})$. The hidden layer $\mathbf{h}$ describes the low-dimensional representation of the input $\mathbf{v}$. The encoder and the decoder are trained by the back-propagation algorithm to minimize a cost function. The dimension of the encoder output (i.e. learned representation) is chosen less than that of the input representation. At the beginning, following the input layer $\mathbf{v}$, the

training data $\tilde{\mathbf{v}}$ is corrupted by Gaussian noise (i.e. producing the corrupted sample $\tilde{\mathbf{v}}$ out of original sample $\mathbf{v}$) which is of the same dimension as $\mathbf{v}$.

A denoising encoder can both reduce the sensitivity to small stochastic data corruption, especially when some input data are missing, and decrease the dimension of the representation which is the input of the classification neural network for the converter instability detection. The learned representation is produced by the encoder at the next layer of M neurons. The layer is constructed by means of the weights w_{ml} that map the contribution of input feature $\tilde{v}_l$ to the hidden layer. Firstly, an affine transformation is performed by

$$z_m = \sum_{l=1}^{L} w_{ml}\tilde{x}_l + b_m \tag{3.16}$$

where L is the number of samples in each time-series of the sampled PCC voltage and b_m is the bias term. Next, a squashing function f is applied to z_m as the encoder activation $h_m = f_{enc}(z_m)$ for each hidden neuron.

At the output layer, the reconstructed representation is produced by adjusting the contribution of the learned representation h_m to the sample feature $\hat{v}_n$ via a set of weights $\hat{w}_{nm}$. The weights $\hat{w}_{nm}$ and a set of biasing parameters $\hat{b}_n$ formulate the affine mapping by

$$\hat{z}_n = \sum_{m=1}^{M} \hat{w}_{nm}h_m + \hat{b}_n \tag{3.17}$$

which is coupled with a decoder squashing function $\hat{v}_n = f_{dec}(\hat{z}_n)$ generates the reconstructed data sample $\hat{\mathbf{v}}$. The neural network parameters can be organized in a series of matrices $\mathbf{W}_{M \times L}$, $\mathbf{b}_{M \times 1}$, $\hat{\mathbf{W}}_{L \times M}$, and $\hat{\mathbf{b}}_{L \times 1}$. The parameter sets can be arranged in the following compact set of equations as

$$\begin{aligned}\mathbf{h}_{M \times 1} &= f\left(\mathbf{W}_{M \times L}\tilde{\mathbf{v}}_{L \times 1} + \mathbf{b}_{M \times 1}\right) \\ \hat{\mathbf{v}}_{L \times 1} &= f\left(\hat{\mathbf{W}}_{L \times M}\mathbf{h}_{M \times 1} + \hat{\mathbf{b}}_{L \times 1}\right).\end{aligned} \tag{3.18}$$
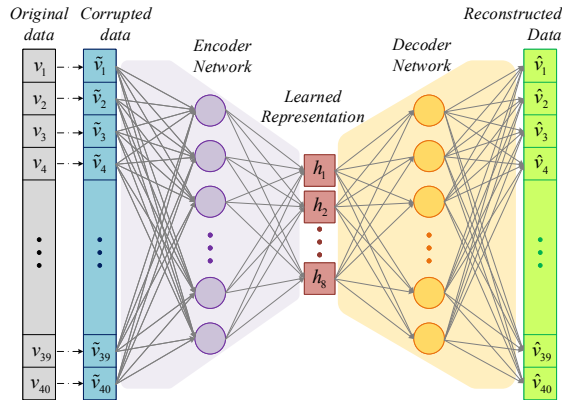

Figure 3.11. Denoising autoencoder.

The squashing function f can be applied element-wise to vectors. The associated reconstruction cost function to be minimized regarding to the training data sample $\tilde{\mathbf{v}}$ is expressed by

$$J\left(\mathbf{W}, \mathbf{b}, \hat{\mathbf{W}}, \hat{\mathbf{b}}\right) = \frac{1}{L}\|\mathbf{v} - \hat{\mathbf{v}}\|^2. \tag{3.19}$$

The denoising autoencoder minimizes the cost function which is obtained by comparing the reconstructed representation $\hat{\mathbf{v}}$ with the unelaborated representation $\mathbf{v}$. Consequently, the denoising autoencoder can reverse the corruption. Performing gradient descent for updating the network parameters with the objective of minimizing the reconstruction error is carried out by

$$
\begin{aligned}
\mathbf{W}^{next} &= \mathbf{W}^{current} - \alpha \nabla_W J\left(\mathbf{W}, \mathbf{b}, \hat{\mathbf{W}}, \hat{\mathbf{b}}\right) \\
\mathbf{b}^{next} &= \mathbf{b}^{current} - \alpha \nabla_b J\left(\mathbf{W}, \mathbf{b}, \hat{\mathbf{W}}, \hat{\mathbf{b}}\right) \\
\hat{\mathbf{W}}^{next} &= \hat{\mathbf{W}}^{current} - \alpha \nabla_{\hat{W}} J\left(\mathbf{W}, \mathbf{b}, \hat{\mathbf{W}}, \hat{\mathbf{b}}\right) \\
\hat{\mathbf{b}}^{next} &= \hat{\mathbf{b}}^{current} - \alpha \nabla_{\hat{b}} J\left(\mathbf{W}, \mathbf{b}, \hat{\mathbf{W}}, \hat{\mathbf{b}}\right)
\end{aligned}
\tag{3.20}
$$

where α is the learning rate and ∇_W, ∇_b, $\nabla_{\hat{W}}$ and $\nabla_{\hat{b}}$ represent the partial derivatives of $J\left(\mathbf{W}, \mathbf{b}, \hat{\mathbf{W}}, \hat{\mathbf{b}}\right)$ to the parameters $\mathbf{W}$, $\mathbf{b}$, $\hat{\mathbf{W}}$ and $\hat{\mathbf{b}}$, respectively, for the gradient descent equations. The reconstructed data are given in Fig. 3.12 to demonstrate the ability of the trained autoencoder in reconstructing the original data from corrupted data containing added Gaussian noise. A mean squared error (MSE) cost function penalizing reconstructed data $\hat{\mathbf{v}}$ for being dissimilar from the original data $\mathbf{v}$ (without added noise) is defined as

$$MSE = \frac{1}{N \times L} \sum_{i=1}^{N} \sum_{j=1}^{L} (v_{ij} - \hat{v}_{ij})^2 \tag{3.21}$$

where N is the number of the training data-sets. Two different types of activation function have been used in the autoencoder including Sigmoid and Rectified Linear Unit (ReLU). Number of trainable parameters and type of activation function of the autoencoder layers are listed in Table 3.4.

Original data, corrupted data, and reconstructed data of the sampled PCC voltage for two different cases including stable synchronization and unstable synchronization of the converter are depicted in Fig. 3.12.

3.4.2 Visualization of the Learned Representation

Analyzing the data is the first step in developing a predictive model. Using both principal component analysis (PCA) and t-distributed stochastic neighbour embedding (tSNE) algorithm, Publication I explores and visualizes the trained representation. The PCA reduces large datasets into smaller, more manageable ones, while still preserving most of the information. PCA
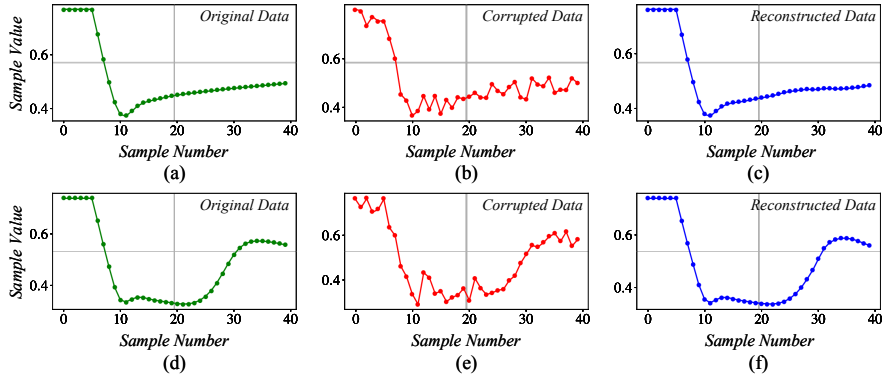
Figure 3.12. Original data, corrupted data, and reconstructed data of the sampled PCC voltage (a) original data for a stable synchronization case, (b) corrupted data with added Gaussian noise for a stable synchronization case, (c) reconstructed data by the trained autoencoder for a stable synchronization case, (d) original data for an unstable synchronization case, (e) corrupted data with added Gaussian noise for an unstable synchronization case, (f) reconstructed data by the trained autoencoder for an unstable synchronization case.

results are plotted in Fig. 3.13 to differentiate between time series labelled as stability in synchronization versus those labelled as instability. The PCA plot illustrates how the PCC voltage time series can be reduced in dimension to detect the synchronization instability of the grid-converter system. Additionally, in the tSNE algorithm, dimensions are eliminated using nonlinear dimension reduction while retaining the structure of the data. Fig. 3.14 shows the tSNE visualizations of the learned representation for both stable and unstable synchronization. More details are provided in Publication I.
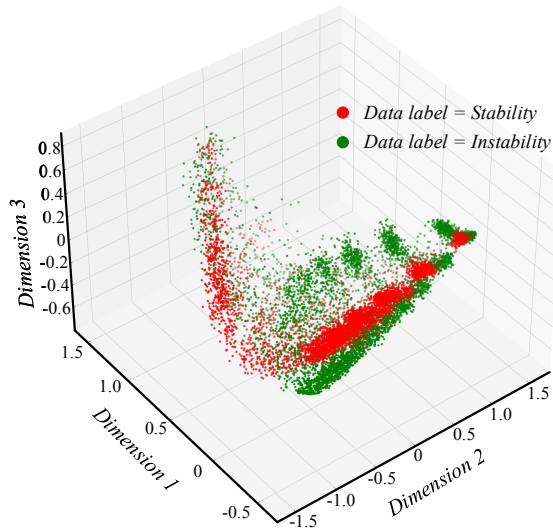

Figure 3.13. PCA plot of the learned representation for 10736 data samples.
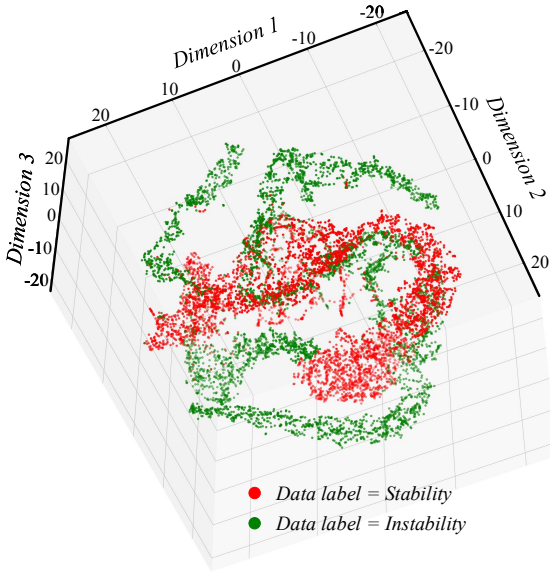
Figure 3.14. tSNE visualization of the learned representation for 10736 data samples.

3.5 Classifier Architecture

In Publication I, an encoder-stacked classifier (ESC) for instability de-
tection is introduced and its performance is compared with conventional
neural networks. Figure 3.15 shows the proposed ESC. For implementing
a traditional neural network, the MLP structure is selected and the speci-
fications are listed in Table 3.4. The employed MLP is a straightforward
neural network architecture with one input layer, two hidden layers, and
an output layer. The employed MLP has a feed-forward architecture where
the neurons in the same layer are not connected to each other. The aim
of the training was to achieve optimum accuracy with MLP. The data set
used for training, validating, and testing both neural networks (i.e. ESC
and MLP) consists of 42944 time series of the PCC voltage samples. The
final layer of the transient instability detection system based on the MLP
is a Softmax classifier similar to the ESC. The Softmax classifier aims
to determine the class of the given test sample and uses a cross-entropy
loss function. By employing the denoising encoder that is trained in the
previous section, the ESC is more robust against artefacts and missing
data.

   The main approach used in Publication I is to interpret the outputs of
the model as probabilities. In this method, $P_{\text{Sta.}}$ represents the probability
of a stable operating point, whereas, $P_{\text{Ins.}}$ denotes the probability of grid-
converter system instability. The parameters of the Softmax are optimized
to produce probabilities that maximize the likelihood of the observed data.
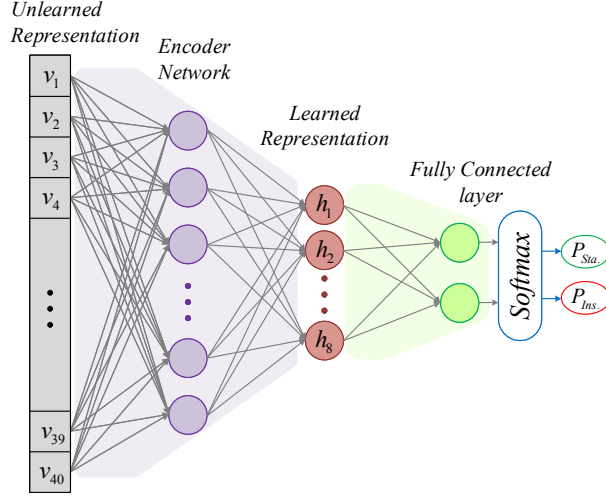Then by setting a threshold and choosing the label with the maximum pre-

Figure 3.15. The proposed encoder stacked classifier.

dicted probability, predictions are generated. This means that a prediction is made based on the class with the highest output value.

3.5.1 Training and Validating ESC and MLP

Specifications of the generated data are listed in Table 3.3. Five variables have been considered in generating the raw data including pre-fault active power of the converter P_{ref}, Voltage sag severity ΔV_{sag}, Voltage sag duration ΔT_{sag}, X/R ratio, and SCR. Resulting in 80000 combinations of various operating points and grid dynamics. The generated data consists of 58528 time-series labelled as *Stable* and 21472 time series labelled as *Unstable*. In order to train both neural networks with balanced distributed data (equal number of stable and unstable cases), 21472 time series have been selected randomly out of the 58528 time series labeled as *Stable*. Consequently, 42944 time series have been allocated for training and testing both ESC and MLP. The share of the training data is equal to 75% and the share of the testing data is equal to 25% of the 42944 time series. Both ESC and MLP have been trained and tested using Keras, Scikit-learn, and TensorFlow libraries in Python and then imported to MATLAB/Simulink to be integrated into PSC, which is described in the following sections. Similar data including added Gaussian noise with the mean value of zero and the standard deviation of 10% have been used for the two classifiers (ESC and MLP).

The confusion matrix of the MLP classifier is presented in Fig. 3.16(a) and the confusion matrix of the ESC is presented in Fig. 3.16(b) for the test data consisting of 5368 time series labelled as *Stable* and 5368 time series labelled as *Unstable*. Both the MLP classifier and the ESC fared

well in prediction accuracy of the noisy data. However, because of the pre-trained denoising encoder, the ESC learned the most salient features of the input data and used these features to present more robustness against artefacts and missing data. The misclass rate of the MLP classifier is almost twice that of the ESC. The encoder in ESC is trained separately in order to reduce the dimension of the original representation and produce a learned representation which is more robust against corrupted data and can be reverted to the original representation by the decoder. The test data used for comparing the accuracy of these two instability detection methods consist of 10736 time series of the PCC voltage samples including same number of stable and unstable cases. Detailed information can be found in Publication I.

3.6   Integrating Instability Detection into PSC

As a GFM control scheme, PSC maintains a constant internal voltage phasor during short-term transients [54]. This is due to PSC's inherent voltage source behaviour, while the converter current responds instantly. Integration of the proposed early instability detection method into PSC, which is demonstrated in Fig. 3.17, prevents loss of synchronization in the grid-converter system. The early instability detection by ESC activates the phase freezing mode of the synchronization loop of PSC. Consequently, by freezing the power angle δ, the converter operates as a constant-frequency voltage source with variable amplitude controlled by the reactive power controller $C_Q(s)$. This type of response helps to form the PCC voltage during severe voltage sags and enables other grid-connected converters that are operating as grid-following (GFL) converters to remain connected to the PCC and support the grid during transients as well.

Freezing the converter power angle δ is a straightforward and practical
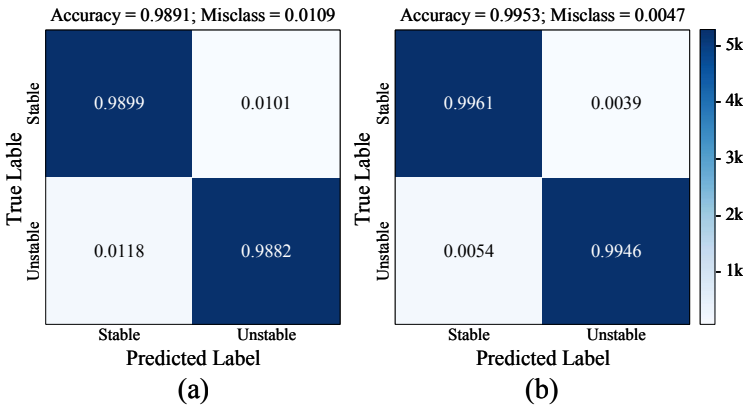

Figure 3.16. Confusion matrix of (a) the MLP-based classifier, and (b) the proposed ESC.
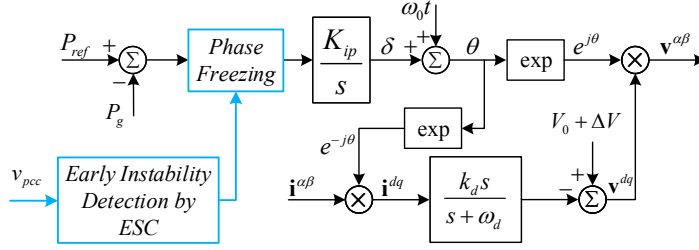
Figure 3.17. Integration of the early instability detection block into the synchronization loop of PSC.

solution to address the loss of synchronization if the converter is connected to a weak grid that does not impose excessive overcurrent on the converter. Freezing the power angle implies that the active power error which is the input of the PSL, given by (2.7), is bypassed by nullifying the active power error following the early detection of the converter instability by ESC and during the grid fault. The synchronization loop output is successfully preserved at the pre-fault frequency.

3.6.1   Parallel Operation of a GFM Converter with a GFL Converter

A GFL converter is typically implemented based on vector control (VC) and phase-locked loops (PLLs) and represented as a current source connected to the grid in parallel with a high impedance. The GFL converter is intended primarily to deliver power to the grid, thus, the current source should be perfectly synchronized with the PCC voltage [54]. In weak grids and during grid faults, the GFL converter will require a voltage source or a GFM converter to support the grid voltage. The parallel operation of a GFM converter and a GFL converter is depicted in Fig. 3.18. Both converters are connected to the same grid and deliver active and reactive power in accordance with grid codes. The GFM converter maintains its internal voltage phasor constants during transients, whereas the GFL converter maintains its internal current phasor constants.

Publication I presents two case studies of GFM and GFL converters operating in parallel during severe voltage sag. The conventional PSC is used in the first case study, and the ESC-integrated PSC is used in the second. At $t = 0.1$ s a three-phase fault occurs in the grid and the grid voltage decreases to 0.4 p.u. subsequently. Time-domain simulations of the two cases are shown in Fig. 3.19 and Fig. 3.20. System parameters used for time-domain simulations are given in Table 3.5, and typical VC is adopted for the GFL converter [55].

Simulation results of parallel operation of the converters for the first case are shown in Fig. 3.19, including the grid three-phase voltage, PCC three-phase voltage, PCC voltage amplitude, power angle of the PSC-controlled
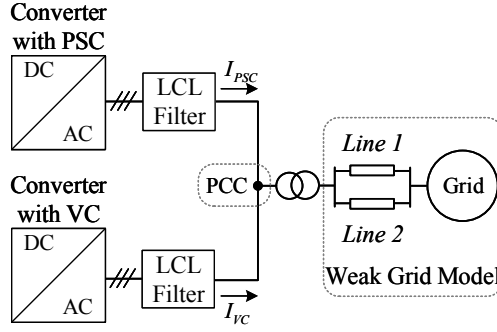
Figure 3.18. Block diagram of the Parallel connection of converters with PSC and VC.

converter, three-phase current of the PSC-controlled converter, and three-phase current of the VC-controlled converter. Due to the voltage sag, the PSC-based converter loses synchronization with the grid, which also leads to inappropriate operation of the parallel VC-based converter. In this case, the PCC voltage fluctuates and the PLL of the VC-based converter is not able to track the voltage properly, thus the output currents of both converters show an unstable response.

Similarly, simulation results of parallel operation of the converters for the second case (ESC-integrated PSC with phase freezing capability) are shown in Fig. 3.20. As a result of the timely detection of synchronization instability and the activation of the phase freezing mode, the GFM converter serves as a constant-frequency voltage source for regulating the PCC voltage and supporting the grid. Furthermore, the GFL converter works properly and helps the PCC voltage recovery by delivering reactive power. The sampling window and phase freezing interval are shown in Fig. 3.20. The phase freezing mode is activated by the ESC and deactivated when the grid voltage recovers.

In Publication I, the results demonstrate that the phase freezing mode can be effective in maintaining synchronization and phase angle stability. Importantly, the GFM converter's power angle δ is frozen only during faults that cause grid-converter instability.

3.7 Harmonic Stability

The interaction between the converter control system and the LCL filter may cause undamped resonances in a wide range of frequencies [56–59]. The harmonic stability of the grid-converter system can be studied by modelling the output impedance of the GFM converter. The harmonic stability of grid-converter systems with PSC is discussed in Publication IV.

Potential resonances would be damped inherently if the converter's output impedance had a phase angle in the range of $[-\pi/2, \pi/2]$. Otherwise, a
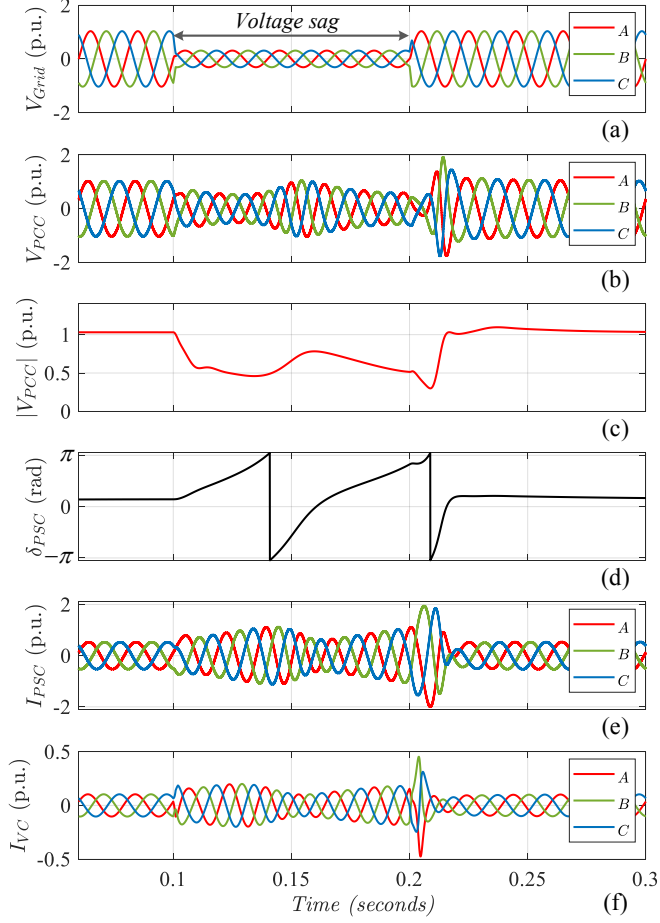
Figure 3.19. Time-domain simulation of parallel operation of converters with conventional PSC and VC without phase freezing capability (a) grid voltage with a 60% voltage sag, (b) PCC voltage, (c) amplitude of the PCC voltage, (d) power angle of the PSC-controlled converter, (e) three-phase current of the PSC-controlled converter, and (f) three-phase current of the VC-controlled converter.

particular selection of sampling frequency, active damping, passive damping, and LCL filter parameters is required. Under certain grid-converter system conditions, harmonic instability can also be caused by the time delay of the converter control system [34, 60]. Therefore, employing an appropriate damping technique is needed to guarantee the stable operation of the converter. In recent years, the use of active damping techniques has gained increasing attention because passive damping techniques contribute to extra power dissipation and inferior efficiency [61–63].

The time delay of the converter control system, which includes sampling, computation, and modulation, introduces a critical frequency of one-sixth of the converter sampling frequency [60]. In weak grid conditions, this time delay implies that the active damping may be ineffective in mitigating
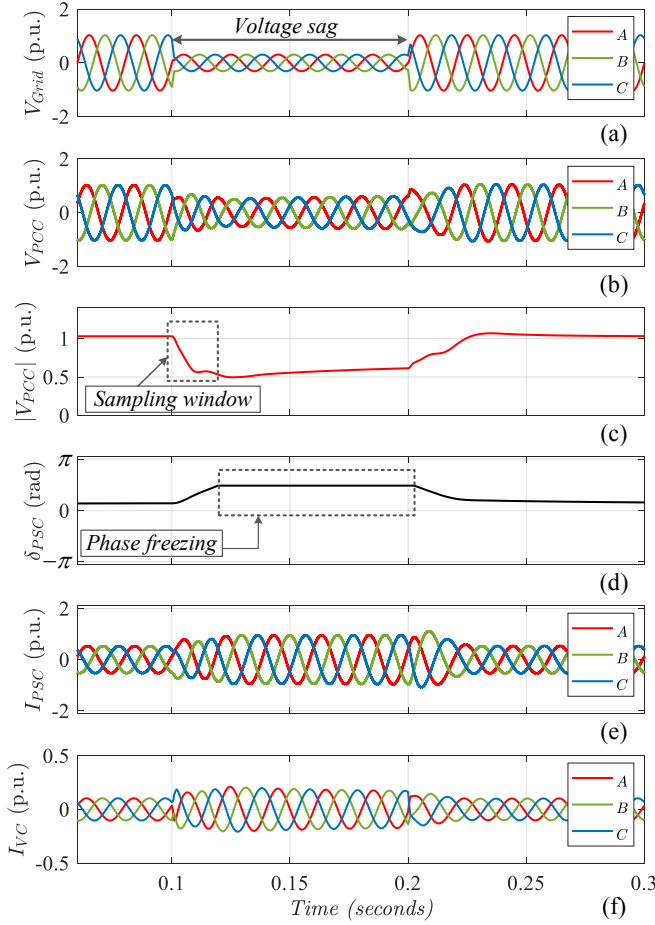
Figure 3.20. Time-domain simulation of parallel operation of converters with developed PSC and VC with phase freezing capability for PSC (a) grid voltage with a 60% voltage sag, (b) PCC voltage, (c) amplitude of the PCC voltage, (d) power angle of the developed PSC-controlled converter, (e) three-phase current of the PSC-controlled converter with phase freezing, and (f) three-phase current of the VC-controlled converter.

certain undamped resonances. Thus, the output impedance of the converter should be modelled by considering the dynamics of the control scheme, the delay and the sampling frequency of the control system, and the linearized model of the grid-converter system. Publication IV presents the linearized model of PSC for harmonic stability assessment.

3.7.1 Modeling Converter Output Admittance

As shown in Fig. 2.2, PSC includes a high-pass filter with a virtual resistance which can be modelled as a current controller $G_D(s)$ for providing damping of high-order current components. In addition, a time delay $G_d(s)$ resulting from the computation and the PWM should be considered to
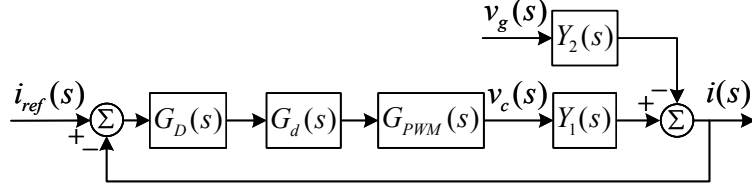
Figure 3.21. Averaged switching model of the grid-connected converter.

model the internal dynamics of PSC. Also, the gain of the PWM can be modelled by $G_{\mathrm{PWM}}(s)$. Thus, an average switching model as depicted in Fig. 3.21 can be obtained by defining

$$
\begin{aligned}
G_{\mathrm{D}}(s) &= R_{\mathrm{d}} \\
G_{\mathrm{d}}(s) &= e^{-1.5 T_{\mathrm{s}} s} \\
G_{\mathrm{PWM}}(s) &= 1
\end{aligned}
\tag{3.22}
$$

where T_{s} is the sampling time of the converter control system. The LCL filter is modelled by neglecting the resistive parts of the passive elements as (2.5) and (2.6). Therefore, the converter output admittance is modelled by $Y_{\mathrm{Conv}}(s)$ as

$$
\begin{aligned}
Y_{\mathrm{Conv}}(s) &= \left. \frac{i_{\mathrm{g}}}{v_{\mathrm{pcc}}} \right|_{i_{\mathrm{ref}}=0} = \frac{Y_2}{1 + G_{\mathrm{c}} G_{\mathrm{d}} Y_1} \\
&= \frac{s^2 C_{\mathrm{f}} L_{\mathrm{fc}} + 1}{s^3 C_{\mathrm{f}} L_{\mathrm{fc}} L_{\mathrm{fg}} + s(L_{\mathrm{fc}} + L_{\mathrm{fg}}) + R_{\mathrm{d}} e^{-1.5 T_{\mathrm{s}} s}}.
\end{aligned}
\tag{3.23}
$$

Considering that the complex admittance network consists of several subsystems, the harmonic stability of the grid-converter system is determined by the relation between the admittances. According to the Nyquist plot, in a stable system with only passive sub-systems, the maximum phase angle should be in the range of $[-\pi, \pi]$, which never encircles $(-1, j0)$. Figure 3.22 shows the bode diagrams of a grid-converter system with LCL filter for two different possible filter parameter selection. The magnitude of the converter output admittance presents a noticeable dip at the anti-resonance frequency ω_{anti} given by

$$
\omega_{\mathrm{anti}} = 1 / \sqrt{C_{\mathrm{f}} L_{\mathrm{fc}}}
\tag{3.24}
$$

which originates from the double zeros of (3.23). Accordingly, three borders are defined to limit the harmonic stability analysis to the relevant frequency range of possible harmonic resonances. The resonance frequency of LCL filter ω_{res}, the critical frequency of the converter ω_{crt} and the Nyquist frequency ω_N of the sampling rate defined by

$$
\begin{aligned}
\omega_{\mathrm{res}} &= \sqrt{\frac{L_{\mathrm{fc}} + L_{\mathrm{fg}}}{L_{\mathrm{fc}} L_{\mathrm{fg}} C_{\mathrm{f}}}} \\
\omega_{\mathrm{crt}} &= \omega_{\mathrm{s}} / 6 \\
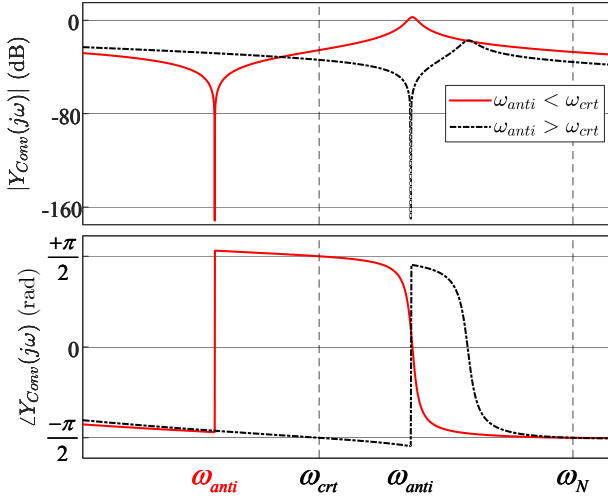\omega_{\mathrm{N}} &= \omega_{\mathrm{s}} / 2
\end{aligned}
\tag{3.25}
$$

Figure 3.22. Bode diagram of the converter output admittance $Y_{\mathrm{Conv}}(s)$ for the two possible LCL-filter selections ($\omega_{\mathrm{anti}} > \omega_{\mathrm{crt}}$ and $\omega_{\mathrm{anti}} < \omega_{\mathrm{crt}}$).

where ω_{s} is the sampling angular frequency of the control system. The critical frequency ω_{crt} is defined as one-sixth of the sampling frequency. In case $\omega_{\mathrm{res}} > \omega_{\mathrm{crt}}$, no resonance damping is required for stable operation of the converter in the stand-alone mode.

The value of the anti-resonance frequency ω_{anti} relative to the critical frequency ω_{crt}, (i.e. $\omega_{\mathrm{anti}} < \omega_{\mathrm{crt}}$ or $\omega_{\mathrm{anti}} > \omega_{\mathrm{crt}}$), causes two classifiable cases in respect to the passive zone of $Y_{\mathrm{Conv}}(s)$ as depicted in Fig. 3.22. The phase angle of $Y_{\mathrm{Conv}}(s)$ exceeds the passive range $[-\pi/2, +\pi/2]$ in the intervals of $(\omega_{\mathrm{anti}}, \omega_{\mathrm{crt}})$ or $(\omega_{\mathrm{crt}}, \omega_{\mathrm{anti}})$. In addition, a phase angle jump occurs due to the time delay introduced by $G_{\mathrm{d}}(s)$.

The non-passive zone can be identified by exploring the real part of the converter output admittance. Real part of $Y_{\mathrm{Conv}}(j\omega)$ can be expressed by

$$
\begin{aligned}
\mathrm{Re}\left\{Y_{\mathrm{Conv}}(j\omega)\right\} &= \frac{R_{\mathrm{d}}\cos(\frac{3\pi}{\omega_{\mathrm{s}}}\omega)(1-\omega^2/\omega_{\mathrm{anti}}^2)}{A^2+B^2} \\
A &= R_{\mathrm{d}}\cos(\tfrac{3\pi}{\omega_{\mathrm{s}}}\omega) \\
B &= R_{\mathrm{d}}\sin(\tfrac{3\pi}{\omega_{\mathrm{s}}}\omega) + \omega(\omega^2 C_{\mathrm{f}}L_{\mathrm{fc}}L_{\mathrm{fg}} - L_{\mathrm{fc}} - L_{\mathrm{fg}}) \\
\omega_{\mathrm{s}} &= 2\pi/T_{\mathrm{s}}.
\end{aligned}
\tag{3.26}
$$

Since the denominator is always positive, the only term that specifies the passivity of the admittance is the cosine term which originates from the time delay $G_{\mathrm{d}}(s)$, and the anti-resonance frequency ω_{anti}. Significant terms of the numerator in (3.26) are plotted in Fig. 3.23. The resultant polarity of $\mathrm{Re}\left\{Y_{\mathrm{Conv}}(j\omega)\right\}$ for three different cases is depicted in Fig. 3.23 as well, which specifies the non-passive zone of the converter output admittance.
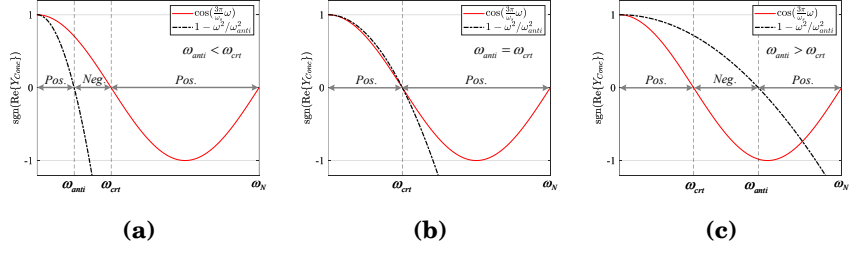
Figure 3.23. Sign of $\mathrm{Re}\,\{Y_{\mathrm{Conv}}(j\omega)\}$ and the passive regions of converter output admittance $Y_{\mathrm{Conv}}(s)$: (a) $\omega_{\mathrm{anti}} < \omega_{\mathrm{crt}}$; (b) $\omega_{\mathrm{anti}} = \omega_{\mathrm{crt}}$; and (c) $\omega_{\mathrm{anti}} > \omega_{\mathrm{crt}}$.
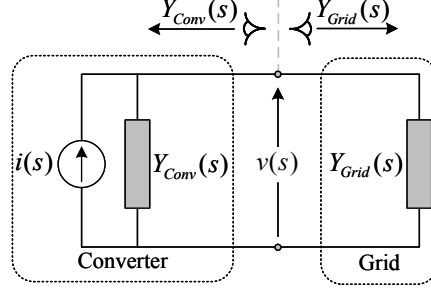

Figure 3.24. Admittance representation of a grid-connected converter for harmonic stability analysis.

3.7.2 Harmonic Stability Analysis of PSC in Weak Power Grids

In grid-converter systems, grid admittance $Y_{\mathrm{Grid}}(s)$ plays a critical role in harmonic stability. The interconnection of the converter output admittance and the grid admittance is shown in Fig. 3.24. Figure 3.25 illustrates the grid-converter system's admittance minor loop $L_{\mathrm{Minor}}(s)$ defined as

$$L_{\mathrm{Minor}}(s) = \frac{Y_{\mathrm{Conv}}(s)}{Y_{\mathrm{Grid}}(s)}. \tag{3.27}$$

Harmonic instability can occur in certain frequency ranges due to non-passive zones of grid-converter admittance. As a result, the critical grid admittance as well as proper operating conditions for achieving harmonic stability in the system should be determined. The minor loop gain $L_{\mathrm{Minor}}(s)$ provides essential insights that can be used to specify constraints for
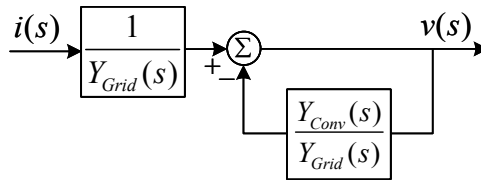

Figure 3.25. Demonstration of the admittance minor loop.

the parameter selection of the LCL filter and the stable operation of the converter.

The harmonic stability of the system can be realized by satisfying two conditions. Firstly, the magnitude condition, and second, the cross-phase crossover condition, expressed as

$$|Y_{\text{Conv}}(j\omega)| > |Y_{\text{Grid}}(j\omega)| \tag{3.28}$$

$$\angle Y_{\text{Conv}}(j\omega) - \angle Y_{\text{Grid}}(j\omega) = -\pi \pm 2n\pi \tag{3.29}$$

Considering an inductive grid admittance, the frequency range of interest is narrowed to the non-passive zone of the converter output admittance. The magnitude of the converter output admittance $|Y_{\text{Conv}}(j\omega)|$ is plotted in Fig. 3.26 and Fig.3.27 for two different cases where $\omega_{\text{anti}} < \omega_{\text{crt}}$ and $\omega_{\text{anti}} > \omega_{\text{crt}}$, respectively. The critical frequency ω_{crt} is where the phase of the converter output admittance $\angle Y_{\text{Conv}}(j\omega)$ crosses $\pm\pi/2$.
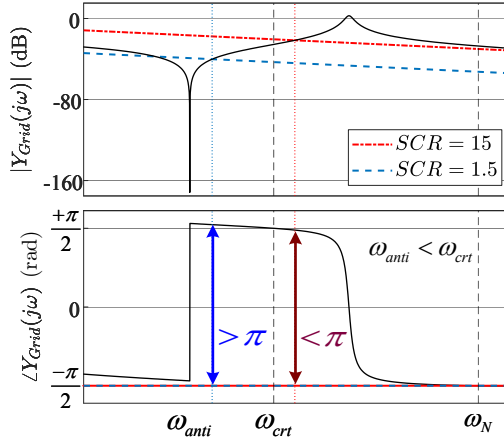

Figure 3.26. Harmonic stability assessment of the grid-connected converter system when $\omega_{\text{anti}} < \omega_{\text{crt}}$ for two different grid SCR values.

Consequently, the magnitude ratio $|Y_{\text{Conv}}(j\omega)| / |Y_{\text{Grid}}(j\omega)|$ at ω_{crt} is the preliminary stage in the harmonic stability assessment. In Publication IV, two SCR values are considered for the grid which represent the strong grid operating condition (SCR = 15) and the very weak grid operating condition (SCR = 1.5). Accordingly, the critical inductance value of the grid can be obtained by matching the grid admittance magnitude $|Y_{\text{Grid}}(j\omega)|$ to the converter output admittance $|Y_{\text{Conv}}(j\omega)|$ at the critical frequency ω_{crt} as

$$Y_{\text{Grid}}(j\omega) = Y_{\text{Conv}}(j\omega)|_{\omega=\omega_{\text{crt}}}. \tag{3.30}$$

By decreasing the SCR value of the grid, the grid admittance line moves downwards as depicted with dashed lines in Fig. 3.26 and Fig. 3.27. In a nutshell, the harmonic stability of the system would be jeopardized in
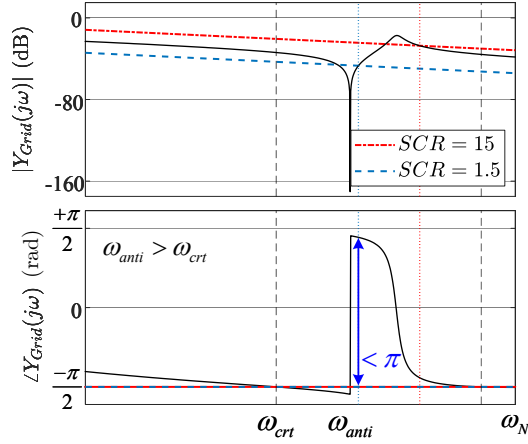
Figure 3.27. Harmonic stability assessment of the grid-connected converter system when $\omega_{\mathrm{anti}} > \omega_{\mathrm{crt}}$ for two different grid SCR values.

weak grids only when ω_{anti} is smaller than ω_{crt} and the grid inductance L_{Grid} is larger than $L_{\mathrm{Grid}}^{\mathrm{crt}}$ defined by

$$
\begin{aligned}
L_{\mathrm{Grid}}^{\mathrm{crt}} &= \frac{\sqrt{A_{\mathrm{crt}}^2 + B_{\mathrm{crt}}^2}}{\omega_{\mathrm{crt}}\left|1 - \omega_{\mathrm{crt}}^2 C_{\mathrm{f}} L_{\mathrm{fc}}\right|} \\
A_{\mathrm{crt}} &= R_{\mathrm{d}} \cos\left(\frac{3\pi}{\omega_{\mathrm{s}}}\omega_{\mathrm{crt}}\right) \\
B_{\mathrm{crt}} &= R_{\mathrm{d}} \sin\left(\frac{3\pi}{\omega_{\mathrm{s}}}\omega_{\mathrm{crt}}\right) + \omega_{\mathrm{crt}}(\omega_{\mathrm{crt}}^2 C_{\mathrm{f}} L_{\mathrm{fc}} L_{\mathrm{fg}} - L_{\mathrm{fc}} - L_{\mathrm{fg}}).
\end{aligned}
\tag{3.31}
$$

The harmonic stability analysis of the grid-converter system is verified by time-domain simulations in Pub IV. The analysis was conducted on two case studies. In the first case, the anti-resonance frequency is smaller than the critical frequency, as shown in Fig. 3.28(a) and (b). In the second case, the anti-resonance frequency is greater than the critical frequency, as shown in Fig. 3.29(c) and (d). The results confirm that when the anti-resonance frequency is greater than the critical frequency $\omega_{\mathrm{anti}} > \omega_{\mathrm{crt}}$, the effect of the grid admittance variation is negligible. Thus, harmonic stability would be achieved due to the inherent damping of harmonic components. The detailed description of the presented results are available in Publication IV.
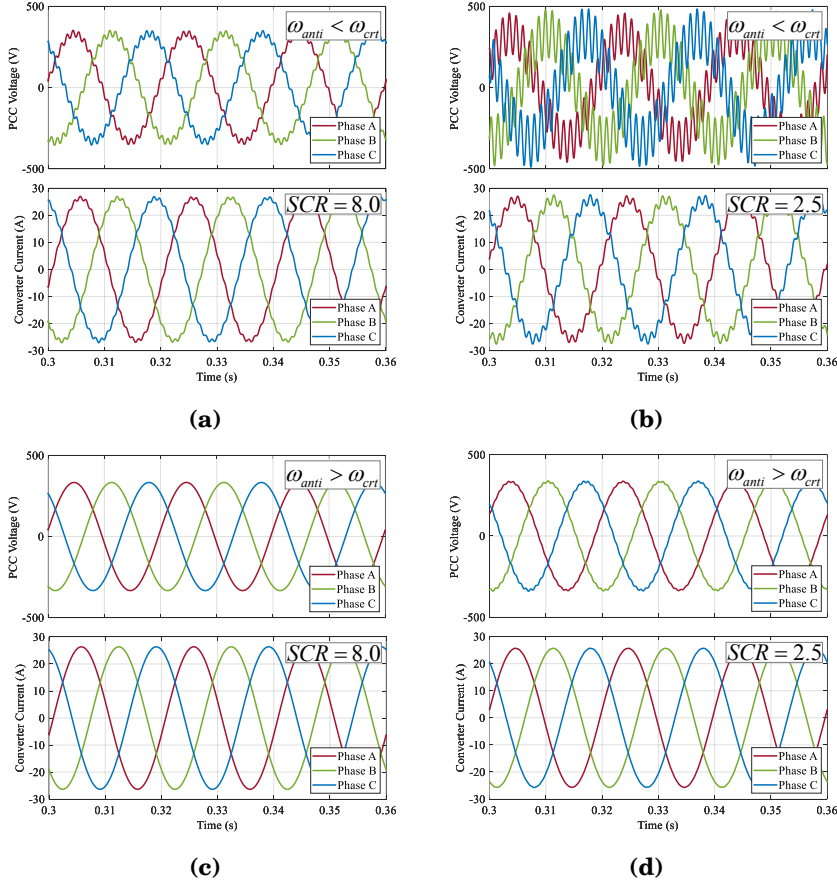
Figure 3.28. Time-domain simulation of the grid-connected converter system for two different grid SCR values: (a) $\omega_{\text{anti}} < \omega_{\text{crt}}$ and SCR=8; (b) $\omega_{\text{anti}} < \omega_{\text{crt}}$ and SCR=2.5; (c) $\omega_{\text{anti}} > \omega_{\text{crt}}$ and SCR=8; and (d) $\omega_{\text{anti}} > \omega_{\text{crt}}$ and SCR=2.5.

Table 3.4. Layer Specifications of Autoencoder, ESC, and MLP

Layer	Type	Shape	Parameters	Activation
Encoder input	Dense	40	1640	ReLU
Encoder output	Dense	8	328	ReLU
Decoder input	Dense	8	72	ReLU
Decoder output	Dense	40	360	Sigmoid
Classifier input	Dense	8	72	ReLU
Classifier output	Dense	2	18	Softmax
MLP input	Dense	40	1640	ReLU
MLP 1st output	Dense	8	328	ReLU
MLP 2nd input	Dense	8	72	ReLU
MLP 2nd output	Dense	2	18	Softmax

Table 3.5. System Parameters for Time-domain Simulations

Parameter	Description	Value
P_{PSC}	Rated power of the converter with PSC	4600 kVA
P_{VC}	Rated power of the converter with VC	1000 kVA
X/R	Reactance to resistance ratio	6
SCR	Short circuit ratio	2.5

4. Experimental Setup

This chapter describes the experimental setup prepared for evaluating the developed control schemes. Additionally, it summarizes the technical specifications of the converter system, the grid simulator, and the weak-grid model. Control system modelling, development and implementation were carried out using MATLAB/Simulink and dSPACE MicroLabBox.

4.1 Setup Description

The back-to-back converter system, shown in Figure 4.1, was prepared for experimental tests. The block diagram of the laboratory setup is depicted in Figure 4.2. The back-to-back converter system includes two 12.5-kVA three-phase frequency converters which are coupled to a common DC link. Two frequency converters (ABB ACS880) and two LCL filters (ABB WFU-02) are used in the back-to-back converter system. The DC-supply converter is connected to the 400-V, 50-Hz grid via an LCL filter and an isolation transformer to supply active power and regulate the DC-link voltage. The test converter (the converter under test) is connected to the weak grid model via an LCL filter. A picture of the experimental setup can be seen in Figure 4.1(a).

The weak-grid model includes an isolation transformer, three resistive-inductive transmission lines with adjustable SCR and X/R, and a Regatron grid simulator. The Regatron grid simulator can be used to simulate various voltage sags, grid faults and unbalanced conditions. In Figure 4.1(b), isolation transformers and resistive-inductive transmission lines are shown.

Further technical data of the back-to-back converter system, the weak-grid model, and the Regatron grid simulator is provided in Table 4.1. Table 4.2 presents the rated parameters of the back-to-back converter system. The rated phase voltages are peak values, and the rated phase currents are peak values.
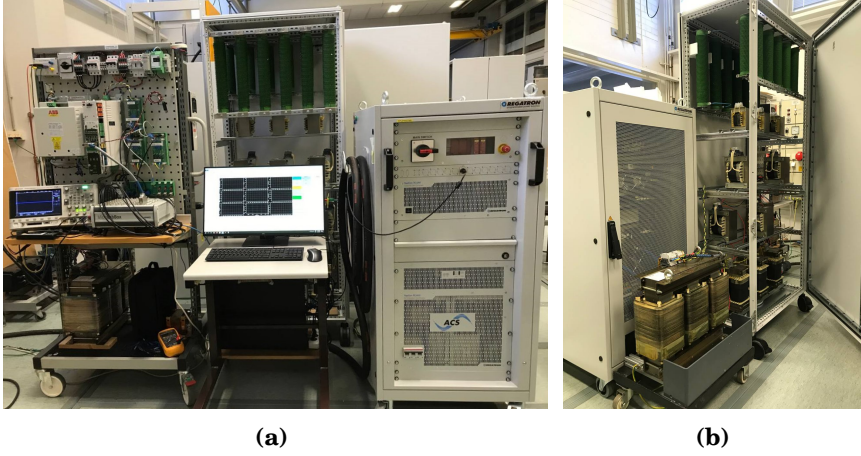
(a)   **(b)**

Figure 4.1. Experimental test setup: (a) back-to-back converter system, dSPACE Micro-LabBox, and Regatron grid simulator; and (b) The isolation transformer and the external resistive-inductive line components.
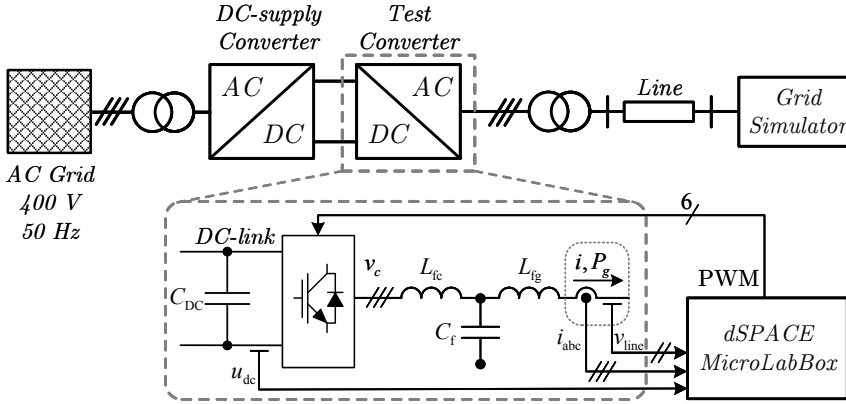

Figure 4.2. Block diagram of the back-to-back converter system and the weak-grid model.

4.2 Implementation

The estimation and control algorithms for the back-to-back converter system were implemented in a dSPACE MicroLabBox development system. The control schemes were initially modelled, developed, and simulated in MATLAB/Simulink, then compiled and transferred to the dSPACE MicroLabBox. The switching signals of the test converter are generated by dSPACE MicroLabBox. The DC-supply converter regulates the DC-link voltage at 650 V and the test converter is controlled by the PSC scheme.

Hall-effect current transducers are used to measure the phase currents. Voltage transducers are used to measure the line voltages and the DC-link voltage as shown in Figure 4.2. The measured variables are sampled with dSPACE MicroLabBox by synchronized sampling method.

Table 4.1. Technical data of the 12.5-kVA back-to-back converter system

Device	Description
Test converter and DC-supply converter	
Frequency converter	ABB ACS880-104-0018A-3
Rated apparent power	12.5 kVA
Rated RMS current	18 A
LCL Filter	
Filter	WFU-02
Measured converter-side inductance L_{fc}	3.0 mH
Measured grid-side inductance L_{fg}	2.0 mH
Filter capacitance C_{f}	10 μF
Grid simulator	
Full 4-quadrant grid simulator	Regatron TopCon TC.ACS
Nominal voltage	400 V
Nominal RMS current	125 A
Weak-grid model	
External inductances ($\times$12)	5, 15, and 25 mH
External resistances ($\times$12)	1.0 and 0.5 Ω
Isolation transformer rated power	25 kVA
Control system	
Prototyping platform	dSPACE MicroLabBox
DC-link voltage measurement	
Voltage sensor	LEM LV 25-1000
Primary voltage measuring range	0 … ±1500 V
Bandwidth	DC … 40 kHz
Line-to-line voltage measurement	
Voltage sensor	LEM LV 25-1000
Primary voltage measuring range	0 … ±900 V
Bandwidth	DC … 40 kHz
Current measurement	
Current sensor	LEM LA 55-P
Primary current measuring range	0 … ±70 A
Bandwidth	DC … 200 kHz

Table 4.2. Rated parameters of the back-to-back converter system

Parameter	Description	Value
Test converter		
V_{peak}	Rated phase voltage (peak)	$230\sqrt{2}$ A
I_{peak}	Rated phase current (peak)	$18\sqrt{2}$ A
U_{DC}	Rated DC-link voltage	650 V
C_{DC}	DC-link capacitance	1.8 mF
Grid		
Z_{base}	Base impedance	12.78 Ω
L_{base}	Base inductance	40 mH
L_{grid}	Grid inductance	5, 15, 20, 25, 30, and 40 mH
R_{grid}	Grid resistance	0.25, 0.5, 1, and 2 Ω

5. Summary of Publications

This chapter presents the abstracts of the publications and the scientific contributions of this thesis.

5.1 Abstracts

The abstracts of the publications are provided in this section.

Publication I

Grid-connected converters are exposed to the loss of synchronisation with the grid during severe voltage sags particularly when operating under weak grid condition which introduces voltage and frequency volatility. This paper presents employing machine learning methods besides modifying the converter control scheme to enhance the transient stability of power synchronization control (PSC). For early detection of synchronization instability of PSC to provide adequate time for taking correcting control actions, an encoder stacked classifier is proposed which is trained to be robust against data corruption and added noise. Then, by integrating the proposed instability detection scheme to the synchronization loop of PSC, a phase freezing mode is introduced to avoid losing synchronism during grid faults. It is disclosed that the frozen synchronization loop, which is activated by the proposed instability detection scheme, can ensure synchronization stability of PSC. Time-domain simulations are conducted to confirm the presented findings.

Publication II

Transient stability of grid-connected converters has become a critical concern to the continuing integration of power electronic converters into the power system. Therefore, this paper aims to study the transient stability of power synchronization control (PSC) and propose a developed control

system by employing deep learning methods. A long short-term memory (LSTM) network has been trained and integrated into PSC for adapting the synchronization loop of the converter to the grid transients. The trained LSTM network extracts and predicts the voltage trajectory of the connection point with respect to the converter dynamics and the grid strength. In the developed control system, active power reference and internal voltage of the converter are updated dynamically to both satisfy the low voltage ride through (LVRT) requirements and prevent the loss of synchronization. The developed control system is validated by time-domain simulation results.

Publication III

Power synchronization control (PSC) has a promising potential to be used in interface converters of large- scale renewable generations operating under weak-grid condition. This paper presents a modified PSC-based control structure that provides an enhanced dynamic response, reinforced synchronization, and reduced vulnerability against grid transients. By utilizing a back-calculation scheme, the active power reference in the synchronization loop of PSC is configured to be adapted to the grid transients for avoiding loss of synchronization (LOS). Furthermore, the proposed control structure prevents power-injection collapse (PIC) and mitigates the dc current components of the converter caused by transients in weak grids. Performance and feasibility of the proposed control structure are highlighted and verified by simulation of various scenarios and operating conditions.

Publication IV

Integration of converter-based resources into weak grids brings new concerns regarding the harmonic stability of modern power systems. This paper studies the harmonic stability and impedance characteristics of power synchronization control (PSC) which has been introduced for control of converters under weak grid operating conditions. This paper addresses this issue by studying the admittance characteristics of PSC based on the dynamics of the control scheme, the delay and the sampling frequency of the control system, and the linearized model of the grid-connected converter. Next, a critical grid inductance is derived, and necessary conditions for achieving harmonic stability are introduced. Time-domain simulations are carried out to support the proposed harmonic stability analysis.

Publication V

Increasing integration of converter-interfaced renewable power generation challenges the stability of the frequency in modern power systems due to the lack of inertia in this type of generation. In this regard, this paper establishes a control method for controlling multilevel converters as an interface between renewable power generation and the power grid, which enables them to operate as voltage-controlled sources, thus grid-forming capabilities like conventional synchronous generators (SGs). In fact, the proposed control technique mimics the behaviour of synchronous generators in the control loop of the neutral point clamped (NPC) converter. Consequently, supportive functionalities for frequency stability i.e., inertia and frequency/power oscillation damping will be provided by the multilevel converter as a virtual synchronous generator (VSG). Simulation results in MATLAB/Simulink verify the well-designed inertia and damping features for the interfaced converter as well as the appropriate performance of the multilevel converter in reducing total harmonic distortion (THD).

Publication VI

Grid-forming virtual synchronous generator (VSG)-based converter has a promising potential to be used as an interfaced converter for high penetration of renewable energy resources. Although emulating inertia and oscillation damping features in the control scheme of converters is possible, the short-circuit behaviour of synchronous machines during fault conditions or other large-signal disturbances is not replicable in these converters, as their semiconductor devices are current-sensitive. This paper proposes a modified control technique for grid-forming VSG-based converters, enabling their fault-ride-through capability during fault situations. The proposed control technique limits the converter current to its allowable amount while preventing windup in the outer control loops. To validate the performance of the proposed control technique, simulation results in MATLAB/Simulink are provided and discussed in detail.

Publication VII

Increasing integration of renewable energy resources emphasizes the importance of the grid-forming virtual synchronous generator (VSG)-based converters. An important issue in the control structure of these converters is the fault ride-through (FRT) capability under fault operating conditions. In this paper, a model predictive-based FRT control strategy is proposed to limit the converter current while ensuring high power quality during fault situations. The proposed control method provides a fast dynamic response, high power quality, improved performance, and a simpler control

structure. The effective performance of the proposed control method, as well as its superior performance in comparison with conventional PI-based control and a model predictive-based control method, are validated through simulation results in MATLAB/Simulink.

5.2 Scientific Contributions

The main scientific contributions of this doctoral thesis are summarized as follows:

- The dynamics of the grid-converter system and the deteriorating influence of the reactive power control loop on the transient stability of PSC during severe voltage sags are studied and explored in Publications I, II, and III. Moreover, various grid dynamics, i.e. a wide range of X/R and SCR values, have been considered to characterize the dynamic response of the grid-converter system in transients and disturbances.

- In Publication I, deep neural networks, autoencoders, and MLP classifiers are proposed as machine learning methods that can be integrated into PSC to enhance grid-converter system transient stability. These methods allow for early detection of synchronization instability, so corrective actions can be taken in a timely manner. The encoder-stacked classifier in these methods is trained to be robust against data corruption and noise. Finally, by integrating the introduced instability detection scheme into PSC, a phase freezing mode is enabled to avoid losing synchronism during grid faults.

- Publication II introduces an LSTM neural network for adapting PSC's synchronization loop to grid voltage transients. As a result of taking into account the converter dynamics and the grid strength, the proposed LSTM neural network extracts and predicts the voltage trajectory of the connection point. Dynamically updating power reference and converter internal voltage ensures compliance with LVRT requirements and prevents loss of synchronization in the developed control system.

- In Publication III, a modified controller is proposed by utilizing a back-calculation scheme in the synchronization loop of PSC in order to overcome the restrictive effect of nonminimum-phase behaviour and the limited bandwidth of PSC. In addition, the proposed controller improves the damping characteristics of PSC against decaying DC components of transient currents.

- Publication IV focuses on the harmonic stability of the grid-converter

system by studying and analyzing the output impedance of the converter over a wide frequency range. As a result of this analysis, a set of criteria is developed for selecting the converter's sampling frequency and filter characteristics in order to enhance harmonic stability.

- Based on the swing equation and power-frequency droop of synchronous machines, publications V, VI, and VII present modified methods for GFM control of converters to provide virtual inertia, fast frequency response, and oscillation damping. By means of these methods, ancillary services can be provided and LVRT capabilities can be implemented in GFM converters.

6. Conclusions and Outlook

This thesis has made several contributions to the ongoing effort of modifying the control and stability of GFM converters in weak power grids. This chapter summarizes those contributions and proposes several potential research paths for the future.

6.1 Conclusions

As distributed power resources are increasingly integrated into modern power systems, GFM converters can be seen as a solution to improve the stability and resilience of weak power systems. However, the dynamic behaviour of the grid-converter systems is strongly influenced by inevitable disturbances and transients in weak power grids. Grid-converter systems are also subject to harmonic instability because of the interaction between the converters and passive components. Therefore, this thesis aimed to improve the transient stability and harmonic stability of grid-converter systems by employing deep-learning and analytic methods. Although this thesis focused on PSC as an appropriate GFM control scheme for weak power grids, the presented methods and analyses can be applied to other GFM control schemes.

In Publication I-IV, the dynamic behaviour of PSC during grid faults is analysed and used to modify the control scheme. First, the back-calculation method is applied and the damping characteristics of PSC are improved to develop the control scheme of ETS-PSC. A modified active power error expression and DC component suppression are included in the ETS-PSC scheme to enhance synchronization against grid transients.

Next, by employing LSTM neural networks in Publication II, a deep-learning method was developed that could provide grid voltage forecasts during grid faults. The LSTM neural network was trained to process and predict the grid voltage trajectory and update the control system's references. A dynamic reference calculation method was also introduced to both satisfy the LVRT requirements and the converter transient stability.

Then, the deteriorating effect of the reactive power control loop was analyzed along with weak grid dynamics in Publication I. Furthermore, Publication I presented both an early instability detection scheme and a control scheme modification using deep learning. Data reconstruction, dimension reduction, and representation learning have been used to train and develop a deep neural network, i.e., a stacked encoder classifier, for early detection of synchronization instability in the grid-converter system. Then, by integrating the proposed early instability detection system into the synchronization loop of PSC and introducing a phase freezing mode, the converter control scheme was modified. The proposed modification prevents losing synchronization with the grid due to severe voltage sags under weak grid operating conditions.

Lastly, the harmonic stability in the grid-converter system with PSC was studied under different case studies in Publication IV. Furthermore, it was revealed that the variation in admittance under weak-grid operating conditions can compromise the harmonic stability of the system. The presented analysis showed that by proper selection of the LCL-filter components regarding the sampling frequency and structure of the control system, it is possible to appropriately diminish the effect of the grid admittance variation on the harmonic stability of the system. In addition, the necessary conditions for achieving harmonic stability have been established.

6.2 Outlook

Considering the contributions of the thesis and the current state of the research field, the author suggests the following potential research directions to proceed:

1. Efforts to enhance the transient stability of grid-converter systems continue to be ongoing, especially given the need for improved stability with the introduction of various GFM control methods in recent years. In this thesis, methods were proposed to enhance the transient stability of the PSC scheme under weak grid conditions. However, as each GFM control system has its unique dynamic behaviour, these methods must be modified to adapt to others. This adaptation will require several modifications, including the development of updated data sets that accurately describe the dynamic behaviour of other GFM control methods as well as larger, variable, and unbalanced networks.

2. The thesis has demonstrated the potential of using machine learning to improve the transient stability of grid-converter systems. With new machine learning algorithms being developed every day, it is possible to further refine and compare the methods described in this

thesis with more advanced approaches. In addition, exploring ways to increase the intelligence of the proposed methods to enhance the contribution of VSG for the stability of the entire electricity network in future power systems, including new types of loads such as electric vehicles, would make for an interesting topic for future research. Moreover, incorporating more advanced machine learning algorithms and exploring additional features that could improve the accuracy and effectiveness of the proposed methods should also be considered.

3. This doctoral research involved setting up a laboratory and implementing back-to-back grid-connected converters. While the machine learning methods proposed in this thesis were applied to simulated grid-converter systems, the next step is to apply and implement these methods in practice using the experimental setup previously prepared. Additionally, the proposed control techniques can be implemented and validated through hardware in the loop (HIL) and power HIL using Typhoon and dSPACE MicroLabBox, which should be part of future research. By doing so, the effectiveness and practicality of these methods can be thoroughly evaluated and validated.

4. The inclusion of current limiting features in grid-forming converters is crucial to maintain the stability and reliability of the power grid. Further research on developing effective current limiting methods for grid-forming converters and expanding their application to MW-range high-voltage converters would pave the way for the continuation of this research work.

References

[1] Roberto Rosso, Xiongfei Wang, Marco Liserre, Xiaonan Lu, and Soenke Engelken. Grid-forming converters: an overview of control approaches and future trends. In *2020 IEEE Energy Conversion Congress and Exposition (ECCE)*, pages 4292–4299, 2020.

[2] Linbin Huang, Huanhai Xin, Zhiyi Li, Ping Ju, Hui Yuan, Zhou Lan, and Zhen Wang. Grid-synchronization stability analysis and loop shaping for pll-based power converters with different reactive power control. *IEEE Transactions on Smart Grid*, 11(1):501–516, 2020.

[3] Mads Graungaard Taul, Saeed Golestan, Xiongfei Wang, Pooya Davari, and Frede Blaabjerg. Modeling of converter synchronization stability under grid faults: The general case. *IEEE Journal of Emerging and Selected Topics in Power Electronics*, 10(3):2790–2804, 2022.

[4] Teng Liu and Xiongfei Wang. Transient stability of single-loop voltage-magnitude controlled grid-forming converters. *IEEE Transactions on Power Electronics*, 36(6):6158–6162, 2021.

[5] Sen Huang, Jun Yao, Jinxin Pei, Shiyue Chen, Yi Luo, and Zhaoyang Chen. Transient synchronization stability improvement control strategy for grid-connected vsc under symmetrical grid fault. *IEEE Transactions on Power Electronics*, 37(5):4957–4961, 2022.

[6] Masoud Davari and Yasser Abdel-Rady I. Mohamed. Robust vector control of a very weak-grid-connected voltage-source converter considering the phase-locked loop dynamics. *IEEE Transactions on Power Electronics*, 32(2):977–994, 2017.

[7] Xiongfei Wang, Mads Graungaard Taul, Heng Wu, Yicheng Liao, Frede Blaabjerg, and Lennart Harnefors. Grid-synchronization stability of converter-based resources—an overview. *IEEE Open Journal of Industry Applications*, 1:115–134, 2020.

[8] Mads Graungaard Taul, Chao Wu, Shih-Feng Chou, and Frede Blaabjerg. Optimal controller design for transient stability enhancement of grid-following converters under weak-grid conditions. *IEEE Transactions on Power Electronics*, 36(9):10251–10264, 2021.

[9] Donghua Pan, Xiongfei Wang, Fangcheng Liu, and Rongliang Shi. Transient stability of voltage-source converters with grid-forming control: A design-oriented study. *IEEE Journal of Emerging and Selected Topics in Power Electronics*, 8(2):1019–1033, 2020.

[10] Javad Khazaei, Zhenghong Tu, Arash Asrari, and Wenxin Liu. Feedback linearization control of converters with lcl filter for weak ac grid integration. *IEEE Transactions on Power Systems*, 36(4):3740–3750, 2021.

[11] Chaoran Yang, Linbin Huang, Huanhai Xin, and Ping Ju. Placing grid-forming converters to enhance small signal stability of pll-integrated power systems. *IEEE Transactions on Power Systems*, 36(4):3563–3573, 2021.

[12] Meng Chen, Dao Zhou, Ali Tayyebi, Eduardo Prieto-Araujo, Florian Dörfler, and Frede Blaabjerg. Generalized multivariable grid-forming control design for power converters. *IEEE Transactions on Smart Grid*, 13(4):2873–2885, 2022.

[13] Meng Chen, Dao Zhou, and Frede Blaabjerg. Enhanced transient angle stability control of grid-forming converter based on virtual synchronous generator. *IEEE Transactions on Industrial Electronics*, 69(9):9133–9144, 2022.

[14] Ebrahim Rokrok, Taoufik Qoria, Antoine Bruyere, Bruno Francois, and Xavier Guillaud. Transient stability assessment and enhancement of grid-forming converters embedding current reference saturation as current limiting strategy. *IEEE Transactions on Power Systems*, 37(2):1519–1531, 2022.

[15] Diptak Pal and Bijaya Ketan Panigrahi. Reduced-order modeling and transient synchronization stability analysis of multiple heterogeneous grid-tied inverters. *IEEE Transactions on Power Delivery*, pages 1–12, 2022.

[16] Xikun Fu, Jianjun Sun, Meng Huang, Zhen Tian, Han Yan, Herbert Ho-Ching Iu, Pan Hu, and Xiaoming Zha. Large-signal stability of grid-forming and grid-following controls in voltage source converter: A comparative study. *IEEE Transactions on Power Electronics*, 36(7):7832–7840, 2021.

[17] Julian Freytes, Jiaqi Li, Guillaume de Préville, and Marc Thouvenin. Grid-forming control with current limitation for mmc under unbalanced fault ride-through. *IEEE Transactions on Power Delivery*, 36(3):1914–1916, 2021.

[18] Mingxuan Li, Yue Wang, Weihao Hu, Sirui Shu, Peng Yu, Zhenyuan Zhang, and Frede Blaabjerg. Unified modeling and analysis of dynamic power coupling for grid-forming converters. *IEEE Transactions on Power Electronics*, 37(2):2321–2337, 2022.

[19] Bo Fan and Xiongfei Wang. Equivalent circuit model of grid-forming converters with circular current limiter for transient stability analysis. *IEEE Transactions on Power Systems*, 37(4):3141–3144, 2022.

[20] Jiantao Zhao, Meng Huang, Han Yan, Chi K. Tse, and Xiaoming Zha. Nonlinear and transient stability analysis of phase-locked loops in grid-connected converters. *IEEE Transactions on Power Electronics*, 36(1):1018–1029, 2021.

[21] Yuan Liu, Jun Yao, Jinxin Pei, Yang Zhao, Peng Sun, Deiyin Zeng, and Shiyue Chen. Transient stability enhancement control strategy based on improved pll for grid connected vsc during severe grid fault. *IEEE Transactions on Energy Conversion*, 36(1):218–229, 2021.

[22] Xiuqiang He, Hua Geng, Ruiqi Li, and Bikash Chandra Pal. Transient stability analysis and enhancement of renewable energy conversion system during lvrt. *IEEE Transactions on Sustainable Energy*, 11(3):1612–1623, 2020.

[23] Xinshuo Wang, Heng Wu, Xiongfei Wang, Laurids Dall, and Jun Bum Kwon. Transient stability analysis of grid-following vscs considering voltage-dependent current injection during fault ride-through. *IEEE Transactions on Energy Conversion*, pages 1–13, 2022.

[24] Tianqiao Zhao, Jianhui Wang, Xiaonan Lu, and Yuhua Du. Neural lyapunov control for power system transient stability: A deep learning-based approach. *IEEE Transactions on Power Systems*, 37(2):955–966, 2022.

[25] Qi Wang, Feng Li, Yi Tang, and Yan Xu. Integrating model-driven and data-driven methods for power system frequency stability assessment and control. *IEEE Transactions on Power Systems*, 34(6):4557–4568, 2019.

[26] Mahdi Khodayar, Guangyi Liu, Jianhui Wang, and Mohammad E. Khodayar. Deep learning in power systems research: A review. *CSEE Journal of Power and Energy Systems*, 7(2):209–220, 2021.

[27] Bowen Zhou, Xiangjin Ma, Yanhong Luo, and Dongsheng Yang. Wind power prediction based on lstm networks and nonparametric kernel density estimation. *IEEE Access*, 7:165279–165292, 2019.

[28] Shuli Wen, Yu Wang, Yi Tang, Yan Xu, Pengfei Li, and Tianyang Zhao. Real-time identification of power fluctuations based on lstm recurrent neural network: A case study on singapore power system. *IEEE Transactions on Industrial Informatics*, 15(9):5266–5275, 2019.

[29] Senlin Zhang, Yixing Wang, Meiqin Liu, and Zhejing Bao. Data-based line trip fault prediction in power systems using lstm networks and svm. *IEEE Access*, 6:7675–7686, 2018.

[30] Mao Tan, Siping Yuan, Shuaihu Li, Yongxin Su, Hui Li, and Feng He. Ultra-short-term industrial power demand forecasting using lstm based hybrid ensemble learning. *IEEE Transactions on Power Systems*, 35(4):2937–2948, 2020.

[31] Mahdi Khodayar and Jianhui Wang. Spatio-temporal graph deep neural network for short-term wind speed forecasting. *IEEE Transactions on Sustainable Energy*, 10(2):670–681, 2019.

[32] Esmaeil Ebrahimzadeh, Frede Blaabjerg, Xiongfei Wang, and Claus Leth Bak. Harmonic stability and resonance analysis in large pmsg-based wind power plants. *IEEE Transactions on Sustainable Energy*, 9(1):12–23, 2018.

[33] Changwoo Yoon, Haofeng Bai, Remus Narcis Beres, Xiongfei Wang, Claus Leth Bak, and Frede Blaabjerg. Harmonic stability assessment for multiparalleled, grid-connected inverters. *IEEE Transactions on Sustainable Energy*, 7(4):1388–1397, 2016.

[34] Xiongfei Wang and Frede Blaabjerg. Harmonic stability in power electronic-based power systems: Concept, modeling, and analysis. *IEEE Transactions on Smart Grid*, 10(3):2858–2870, 2019.

[35] Wenchao Cao, Yiwei Ma, and Fred Wang. Sequence-impedance-based harmonic stability analysis and controller parameter design of three-phase inverter-based multibus ac power systems. *IEEE Transactions on Power Electronics*, 32(10):7674–7693, 2017.

[36] Haitao Zhang, Maryam Saeedifard, Xiuli Wang, Yongqing Meng, and Xifan Wang. System harmonic stability analysis of grid-tied interlinking converters operating under ac voltage control mode. *IEEE Transactions on Power Systems*, 37(5):4106–4109, 2022.

[37] Nagwa F Ibrahim and Sobhy S Dessouky. *Design and Implementation of Voltage Source Converters in HVDC Systems*. Springer, 2021.

[38] Amirnaser Yazdani and Reza Iravani. *Voltage-sourced converters in power systems: modeling, control, and applications*. John Wiley & Sons, 2010.

[39] Chenlei Bao, Xinbo Ruan, Xuehua Wang, Weiwei Li, Donghua Pan, and Kailei Weng. Step-by-step controller design for lcl-type grid-connected inverter with capacitor–current-feedback active-damping. *IEEE Transactions on Power Electronics*, 29(3):1239–1253, 2014.

[40] L. Zhang, L. Harnefors, and H. Nee. Power-synchronization control of grid-connected voltage-source converters. *IEEE Transactions on Power Systems*, 25(2):809–820, 2010.

[41] Lennart Harnefors, Marko Hinkkanen, Usama Riaz, F. M. Mahafugur Rahman, and Lidong Zhang. Robust analytic design of power-synchronization control. *IEEE Transactions on Industrial Electronics*, 66(8):5810–5819, 2019.

[42] Gilbert Bergna-Diaz, Jon Are Suul, and Salvatore D'Arco. Energy-based state-space representation of modular multilevel converters with a constant equilibrium point in steady-state operation. *IEEE Transactions on Power Electronics*, 33(6):4832–4851, 2018.

[43] Lennart Harnefors, F. M. Mahafugur Rahman, Marko Hinkkanen, and Mikko Routimo. Reference-feedforward power-synchronization control. *IEEE Transactions on Power Electronics*, 35(9):8878–8881, 2020.

[44] Mads Graungaard Taul, Xiongfei Wang, Pooya Davari, and Frede Blaabjerg. Current limiting control with enhanced dynamics of grid-forming converters during fault conditions. *IEEE Journal of Emerging and Selected Topics in Power Electronics*, 8(2):1062–1073, 2020.

[45] H. Wu and X. Wang. Design-oriented transient stability analysis of pll-synchronized voltage-source converters. *IEEE Transactions on Power Electronics*, 35(4):3573–3589, 2020.

[46] Heng Wu and Xiongfei Wang. Design-oriented transient stability analysis of grid-connected converters with power synchronization control. *IEEE Transactions on Industrial Electronics*, 66(8):6473–6482, 2019.

[47] Huijie Cheng, Zhikang Shuai, Chao Shen, Xuan Liu, Zuyi Li, and Z. John Shen. Transient angle stability of paralleled synchronous and virtual synchronous generators in islanded microgrids. *IEEE Transactions on Power Electronics*, 35(8):8751–8765, 2020.

[48] X. He, H. Geng, and S. Ma. Transient stability analysis of grid-tied converters considering pll's nonlinearity. *CPSS Transactions on Power Electronics and Applications*, 4(1):40–49, 2019.

[49] M. G. Taul, X. Wang, P. Davari, and F. Blaabjerg. An overview of assessment methods for synchronization stability of grid-connected converters under severe symmetrical grid faults. *IEEE Transactions on Power Electronics*, 34(10):9655–9670, 2019.

[50] David Infield and Leon Freris. *Renewable energy in power systems*. John Wiley & Sons, 2020.

[51] Behnam Farsi, Manar Amayri, Nizar Bouguila, and Ursula Eicker. On short-term load forecasting using machine learning techniques and a novel parallel deep lstm-cnn approach. *IEEE Access*, 9:31191–31212, 2021.

[52] Mamoun Alazab, Suleman Khan, Somayaji Siva Rama Krishnan, Quoc-Viet Pham, M. Praveen Kumar Reddy, and Thippa Reddy Gadekallu. A multidirectional lstm model for predicting the stability of a smart grid. *IEEE Access*, 8:85454–85463, 2020.

[53] Chia-Tse Lee, Che-Wei Hsu, and Po-Tai Cheng. A low-voltage ride-through technique for grid-connected converters of distributed energy resources. *IEEE Transactions on Industry Applications*, 47(4):1821–1832, 2011.

[54] Roberto Rosso, Markus Andresen, Soenke Engelken, and Marco Liserre. Analysis of the interaction among power converters through their synchronization mechanism. *IEEE Transactions on Power Electronics*, 34(12):12321–12332, 2019.

[55] Agustí Egea-Alvarez, Sajjad Fekriasl, Fainan Hassan, and Oriol Gomis-Bellmunt. Advanced vector control for voltage source converters connected to weak grids. *IEEE Transactions on Power Systems*, 30(6):3072–3081, 2015.

[56] Jacky Chun-Tak Lai, Henry Shu-Hung Chung, Yuanbin He, Weimin Wu, and Frede Blaabjerg. Wideband series harmonic voltage compensator for enhancing stability of microgrids. *IEEE Transactions on Power Electronics*, 37(8):9687–9702, 2022.

[57] Jingrong Yu, Xianfu Lin, Dongran Song, Ruoxue Yu, Yan Li, and Mei Su. Harmonic instability and amplification for grid-connected inverter with voltage harmonics compensation considering phase-locked loop. *IEEE Journal of Emerging and Selected Topics in Power Electronics*, 8(4):3944–3959, 2020.

[58] Pankaj D. Achlerkar and Bijaya Ketan Panigrahi. Dynamic harmonic domain modeling and stability augmented design of inverter interface to weak and unbalanced grid. *IEEE Transactions on Power Delivery*, 37(4):3097–3110, 2022.

[59] Qiang Qian, Shaojun Xie, Liuliu Huang, Jinming Xu, Zhao Zhang, and Binfeng Zhang. Harmonic suppression and stability enhancement for parallel multiple grid-connected inverters based on passive inverter output impedance. *IEEE Transactions on Industrial Electronics*, 64(9):7587–7598, 2017.

[60] Ali Akhavan, Saeed Golestan, Juan C. Vasquez, Josep M. Guerrero, and Chuan Xie. Stability enhancement of inverters in grid-connected microgrids using fir filter. *IEEE Journal of Emerging and Selected Topics in Industrial Electronics*, 2(2):122–131, 2021.

[61] Sreedhar Madichetty, Abhijit Dasgupta, Sambeet Mishra, Chinmoy Kumar Panigrahi, and Ghouse Basha. Application of an advanced repetitive controller to mitigate harmonics in mmc with apod scheme. *IEEE Transactions on Power Electronics*, 31(9):6112–6121, 2016.

[62] Ke Ji, Guangfu Tang, Jie Yang, Yunfeng Li, and Dong Liu. Harmonic stability analysis of mmc-based dc system using dc impedance model. *IEEE Journal of Emerging and Selected Topics in Power Electronics*, 8(2):1152–1163, 2020.

[63] Xiongfei Wang, Frede Blaabjerg, and Weimin Wu. Modeling and analysis of harmonic stability in an ac power-electronics-based power system. *IEEE Transactions on Power Electronics*, 29(12):6421–6432, 2014.

BUSINESS +
ECONOMY

ART +
DESIGN +
ARCHITECTURE

SCIENCE +
TECHNOLOGY

CROSSOVER

DOCTORAL
THESES